Available online at www.sciencedirect.com
ScienceDirect
International Journal of Multiphase Flow 33 (2007) 1–39
International Journal of Multiphase Flow
www.elsevier.com/locate/ijmulflow

Towards large eddy simulation of isothermal two-phase flows: Governing equations and *a priori* tests

E. Labourasse [a,1], D. Lacanette [b], A. Toutant [a,1], P. Lubin [b], S. Vincent [b,2], O. Lebaigue [a,*,1], J.-P. Caltagirone [b], P. Sagaut [c,3]

[a] *LMDL (Laboratoire de Modélisation et de Développement de Logiciels), CEA Grenoble – DEN/DER/SSTH, 17 rue des Martyrs – 38054 Grenoble Cedex 9, France*
[b] *Laboratoire TREFLE (Transferts, Ecoulements, Fluides, Energétique), UMR CNRS 8508 – Site ENSCPB, 16 avenue Pey Berland – 33607 Pessac Cedex, France*
[c] *LMM (Laboratoire de Modélisation en Mécanique), UMPC/CNRS, Boite 162, 4 place Jussieu – 75252 Paris Cedex 05, France*

Received 15 August 2004; received in revised form 7 May 2006

Abstract

This article reports on the potential of application of LES in the calculation of turbulent two-phase flows, in the case where each phase is resolved and interfaces remain much larger than the mesh size. In comparison with single-phase flow, successful application of LES to resolve two-phase flow problems should account for the complex interaction between turbulence and interfaces. Non-linear transfers of turbulent energy across the interface have to be accurately modeled. The derivation of the complete filtered two-phase flow governing equations has been formulated to deal with turbulence at the interface in a comprehensive and practical way. Explicit filtering of 2D direct numerical simulations has been employed to evaluate the order of magnitude of the new subgrid contributions. A parametric study on the academic test case of two counter-rotative vortices and a more complex test case of phase inversion in a closed box have been utilized to perform an order of magnitude analysis of different transport mechanisms. Important features of turbulent energy transfer across the interface have been discussed. Analyses of the numerical results have been conducted to derive conclusions on the relative importance of the different subgrid scale contributions, and modeling issues and solutions are provided.

Keywords: Multiphase flow; Turbulent flow; Large eddy simulation; Subgrid-scale modeling; Energy transfers

* Corresponding author. Tel.: +33 4 38 78 36 70; fax: +33 4 38 78 50 36.
E-mail addresses: vincent@enscpb.fr (S. Vincent), olivier.lebaigue@cea.fr (O. Lebaigue), sagaut@lmm.jussieu.fr (P. Sagaut).
[1] Research supported as a contribution to the MATHY, project by the CEA/DEN (Commissariat à l'Energie Atomique, Directorate of Nuclear Energy).
[2] Tel.: +33 5 40 00 27 07; fax: +33 5 40 00 66 68.
[3] Tel.: +33 1 44 27 54 68; fax: +33 1 44 27 52 59.

0301-9322/$ - see front matter © 2006 Elsevier Ltd. All rights reserved.
doi:10.1016/j.ijmultiphaseflow.2006.05.010

1. Introduction

Many industrial and environmental applications involve high Reynolds number turbulent multiphase flows. Examples include spray formations, oil transportation, sea aerosol formation and many others. A great deal of research efforts has been oriented towards the numerical modeling of multiphase turbulent flows.

The great majority of numerical computations have adopted Reynolds Averaged Navier–Stokes (RANS) modeling. Classical single-phase turbulence models have been used in one or in the two phases without direct consideration of the influence of the multiphase topology of the flow on the turbulence behavior. Sato and Sekoguchi (1975) derived a mixing length model thanks to a void fraction consideration for bubbly channel flows, by splitting the turbulence into shear and multiphase induced turbulence. Some interesting comparisons between classical RANS modeling for two-phase flows have been reported for instance by Homescu and Panday (1999) for condensation on a horizontal tube.

Large eddy simulation (LES) has been also utilized for multiphase flow calculations. A quite large amount of these works deal with particles laden flows or sprays, involving particles even smaller than the Kolmogorov scale (see for instance the works of Boivin et al., 2000; Eaton and Fessler, 1994; Elghobashi et al., 1984; Lain et al., 2002; Menon et al., 1996; Squires and Yamazaki, 1995). Very interesting advances have been made in this scope, that is in the case of one of the two phases is very dispersed, and no large inclusion is present. An other very studied scope is the case of indeformable free surface of an open channel flow. See, e.g., the description of the near free surface turbulence that Calmet and Magnaudet (2003) deduced from their LES and the subgrid scales modeling of Shen and Yue (2001). In all these precedent cases just one of the two phases is resolved and there is no really two-way coupling between each phase and the interface. Our purpose deals rather with the less explored field of deformable interfaces and LES, including interfaces much larger than the mesh size. In term of resolution, that means the interfaces are mainly resolved, whereas not perfectly, and at least a part of the turbulence field is subgrid. This problem is quite different, because both phases can be turbulent, and turbulent energy exchange between the two phases may occur. Christensen and Deigaard (2001) and Watanabe and Saeki (2002) adopted a standard LES model coupled with a Volume of Fluid (VOF) free surface approach for modeling wave breaking. Moreover, Lakehal et al. (2002) derived a subgrid scale model based on the analytical analysis of Drew and Lahey (1987) on the forces acting on a sphere and on the scale similarity principle of Bardina et al. (1983). However, in the above-mentioned models, the impact of the multiphase topology of flow on the turbulent characteristics has never been carefully studied, and the modeling (RANS or LES) is mainly based on analytical considerations. More precise studies on the effect of the dispersed phase on the turbulence evolution are expected to validate the subgrid scale or the Reynolds modeling of turbulence–interface interaction.

For better understanding of these phenomena, Direct Numerical Simulation (DNS) of multiphase flow has been carried out. Some interesting two-dimensional DNS of bubbly flow have been presented by Esmaeeli and Tryggvason (1996), Esmaeeli and Tryggvason (1998, 1999). They studied the relative displacement of an array of slightly deformable bubbles at low Reynolds numbers and show the effect of the bubble wake induced turbulence on the energy spectrum. Fulgosi et al. (2003) used DNS to calculate a sheared air–water flow on a slightly deformable interface. The interest was focused on the effect of the moving interface on the turbulence of the gas phase. They observe that the moving interface modifies the turbulent behavior in comparison with a solid wall. They reported a reduction of the classical anisotropy and an increase in turbulent transfer due to the surface. Experimental studies have also confirmed the strong turbulence–interface interaction. For instance, Lance and Bataille (1991) observe a modification of the classical energy spectra for sufficiently high void fractions. These works enlighten the importance of the turbulence–interface interaction for the phenomenology of turbulence in two-phase flows dynamics.

The objective of the present work is twofold: to formulate in a convenient way the theoretical basis of the spatial filtering of the conservation equations in the framework of multiphase flows with large (i.e. much larger than the mesh size) deformable interface, and to provide a sharp description of the unresolved small scale contributions in the case of LES or RANS modeling, through the examples of interaction between turbulence and deformable interfaces. The critical and peculiar phenomenon of two-phase flows turbulence is the modification of the interfacial transfers. These transfers are of great importance, because they interact at once with the dynamic of the bubble and with the heat transfer (and then the phase change). Thus, we wish to suggest a

new strategy to analyze the two-way coupling between turbulence and interfaces, in focusing on the subgrid transfers through the interface. In this scope, the fundamental cases of vortex–bubble interaction and of the phase-inversion in a closed box have been studied to draw conclusions on the reciprocal effect of the turbulence action on interfaces. These two cases have been carefully selected in order to cover a large range of applications for two-phase flows with large interfaces.

The present article has been organized as follows: Section 1 focuses on the mathematical formalism of the filtered system of multiphase equations. A general formulation dedicated to LES or RANS calculation is provided, and different ways of writing the system of equations are discussed. In Section 2, new terms resulting from this formulation have been identified and discussed in the case of RANS or LES modeling. Scopes for further studies on closure models have been discussed. The numerical methods are shortly described in Section 3. Section 4 presents the two test cases dedicated to the impact of two counter-rotating vortices with a bubble and to the phase inversion in a closed box. Some DNS results and phenomenological analysis of the two academic configurations are provided, in particular in terms of kinetic energy distribution. In Section 5, filters of different sizes are applied to the test cases in order to evaluate the subgrid contributions. The different contributions arising in the LES equations are compared and highlight the modeling requirements of the subgrid contributions. Finally, classical one-phase closure models are tested against the equivalent subgrid contributions. Particular features of the LES for two-phase flows and perspectives are finally drawn.

2. Mathematical formalism

Expecting to lead numerical experiments of turbulent free surface flows, our first aim is to envisage the motion equations for multiphase flows by carrying out, in parallel, spatial filterings associated to both turbulence (see Sagaut, 2003) and phase presence (see Drew, 1983; Magnaudet, 1997). To perform this modeling, we need a completely general formulation of the filtered equations. Many authors have worked on a statistical or LES formulation of the equations. The mathematical formalism used in this paper issues from the work of Ishii (1975) and is called the two-fluid model. In this formulation, the exact interaction between the phases is not explicitly expressed but modeled in the form of an equivalent term. Magnaudet (2000) proposed a more general formulation. However, they considered some subgrid scale terms as negligible. In this study, we formulate turbulent and interface contributions resulting from the filtering and averaging procedures.

2.1. Unfiltered equations

In a multiphase flow consisting of k phases, let us denote the domain occupied by the kth phase as $\mathscr{D}^k$. The most general formulation of conservation of mass and momentum for each phase is given by

(1) Mass:

$$\frac{\partial \rho^k}{\partial t} + \nabla \cdot (\rho^k u^k) = 0 \tag{1}$$

where ρ accounts for the density, u for the velocity and t for the time.

(2) Momentum:

$$\frac{\partial \rho^k u^k}{\partial t} + \nabla \cdot (\rho^k u^k \otimes u^k + p^k \,\mathrm{Id}) - \rho^k g = \nabla \cdot \tau^k \tag{2}$$

where g is gravity, Id stands for the identity tensor, and τ^k is the deviatoric stress tensor, defined by

$$\tau^k = \mu^k \underbrace{\left(S^k - \frac{1}{3}\mathrm{tr}(S^k)\,\mathrm{Id} \right)}_{S_D^k} \tag{3}$$

where tr accounts for the trace of a tensor and S is the deformation rate:

$$S = \nabla u + \nabla^{\mathrm{T}} u \tag{4}$$

It is worth noting that in the most general case, the interface has to be considered as a material surface (in the presence of surfactants) and thus has its own density and momentum. However, in this work, we assume that the density of the interface is always zero. Therefore, the following so-called jump conditions can be applied (see Delhaye, 1974)

(1) Mass: The mass transfer $\dot{m}$ of the kth phase at the interface is defined by

$$\dot{m}^k = \rho^k (u^k - W) \cdot n^k \tag{5}$$

where n accounts for the outgoing normal at the interface. The mass balance for all phases can then be written as

$$\sum_k \dot{m}^k = \sum_k (\rho^k (u^k - W) \cdot n^k) = 0 \tag{6}$$

where W is the speed of displacement of the interface.

(2) The balance of momentum at the interface reads:

$$\sum_k (u^k \dot{m}^k - n^k \cdot (-p^k \,\mathrm{Id} + \tau^k)) = \sigma n^k \nabla_s \cdot n^k - \nabla_s \sigma \tag{7}$$

where ∇_s is the surface derivative operator along the interface and σ is the associated surface tension.

To work with this formalism, it is convenient to extend the definition of each phase to the whole domain (in order, for instance, to use non-conditional boundary conditions for each phase). In order to properly define these extensions, we have to introduce a definition of the interface of the kth phase, as a function of position and time. The interface corresponds to a $n-1$ dimensional restriction of the n dimensional space and can then formally be defined as a function f^k of space and time as follows:

$$x \in \text{the interface} \Longleftrightarrow f^k(x,t) = 0 \tag{8}$$

The function f^k is chosen in order to respect the inequalities:

$$\begin{aligned} x \in \text{the } k\text{th phase} &\Longleftrightarrow f^k(x,t) > 0 \\ x \notin \text{the } k\text{th phase} &\Longleftrightarrow f^k(x,t) < 0 \end{aligned} \tag{9}$$

The sharp phase indicator χ^k can then be defined as

$$\chi^k = h[f^k] \tag{10}$$

where h is the Heaviside function.

This indicator has several useful properties:

$$\sum_k \chi^k = 1 \tag{11}$$

$$\chi^m \chi^n = \delta_{mn} \chi^m \tag{12}$$

$$\nabla \chi^k = -n^k \delta_i \tag{13}$$

Furthermore, χ^k follows an evolution equation:

$$\frac{\partial \chi^k}{\partial t} - W \cdot n^k \delta_i = 0 \tag{14}$$

where δ_i is defined as the Dirac function centered on the interface. Each interface is considered as the intersection surface between different subdomains $\mathscr{D}^k$. The behavior of each phase for points near the boundary of the subdomains $\mathscr{D}^k$ can be easily described using δ_i. Note that reciprocally, δ_i can be expressed as a function of χ^k and n^k:

$$\delta_i = -n^k \cdot \nabla \chi^k \tag{15}$$

Using Eqs. (6)–(14), the governing Eqs. (1) and (2) for the phase-weighted variables can be written as

(1) Mass:

$$\frac{\partial \chi^k \rho^k}{\partial t} + \nabla \cdot (\chi^k \rho^k u^k) = \rho^k (W - u^k) \cdot n^k \delta_i \tag{16}$$

(2) Momentum:

$$\frac{\partial \chi^k \rho^k u^k}{\partial t} + \nabla \cdot (\chi^k [\rho^k u^k \otimes u^k + p^k \,\mathrm{Id} - \tau^k]) - \chi^k \rho^k g = (\rho^k u^k \otimes (W - u^k) - p^k \,\mathrm{Id} + \tau^k) \cdot n^k \delta_i \tag{17}$$

The jump conditions defined by Eq. (5) appears explicitly in Eqs. (16) and (17).

The system of governing equations defined by Eqs. (16) and (17) has to be closed owing to thermodynamic relations. The dynamic viscosity μ can be classically assumed as a function of temperature only.

2.2. The exact one-fluid formulation for multiphase flows

A one-fluid formulation for solving multiphase flows can be obtained by introducing the exact one-fluid variable that is defined as the sum of the phase indicator weighted phases:

$$\phi = \sum_k \chi_k \phi_k \tag{18}$$

Summing Eqs. (16) and (17) on all the phases of the flow, the so-called one-fluid mass and momentum conservation equations are written as

(1) Mass:

$$\frac{\partial \rho}{\partial t} + \nabla \cdot (\rho u) = \sum_k \rho^k (W - u^k) \cdot n^k \delta_i \tag{19}$$

This equation can be simplified using mass jump condition (6) as follows:

$$\frac{\partial \rho}{\partial t} + \nabla \cdot (\rho u) = 0 \tag{20}$$

(2) Momentum:

$$\frac{\partial \rho u}{\partial t} + \nabla \cdot (\rho u \otimes u + p \,\mathrm{Id} - \tau) - \rho g = \sum_k (\rho^k u^k \otimes (W - u^k) - p^k \,\mathrm{Id} + \tau^k) \cdot n^k \delta_i \tag{21}$$

Using the momentum jump condition (7), Eq. (21) becomes

$$\frac{\partial \rho u}{\partial t} + \nabla \cdot (\rho u u + p \,\mathrm{Id} - \tau) - \rho g = \nabla_s \cdot n^k \sigma n^k \delta_i - \nabla_s \sigma \delta_i \tag{22}$$

(3) The transport equation for χ does not give further information, since the equality $\sum_k (n^k \delta_i) = 0$ is obvious.

The one-fluid formulation has been introduced by Kataoka (1986). It allows the implementation of classical one-phase numerical tools for solving multiphase flow problems.

2.3. Filtering and averaging point of view

The previous set of unfiltered equations cannot be used in discrete form unless the resolution scale of the mesh is smaller than the Kolmogorov scale, which is unsuitable for practical applications. The number of degrees of freedom is commonly reduced using filtering or averaging based numerical approaches. In order

to derive a general formalism that is applicable for both approaches, the statistical average or spatial filtering operator is denoted as G. Filtering or averaging over discontinuities is a bit ambiguous. As showed by Sagaut and Germano (2005), this process induces a spurious term due to the jump of the filtered quantities. However, many of the numerical methods commonly used to simulate two-phase flows (like Volume of Fluid, Front-Tracking or the Level Set methods) work with interfaces crossing the cells of the mesh. It means that, if no specific treatment is adopted, the jump condition is also smoothed on at least the size of the cells. It is to reproduce this phenomenon we decide to apply the filter over the discontinuity and not only on each phase independently.

The filtered velocity field is then given by

$$\overline{u(x,t)} = G \bigstar u \tag{23}$$

The properties common to the filtering and averaging approaches have been used to obtain a general filtered/averaged formalism.

In LES modeling, Eq. (24) represents the low-pass frequency filtering of the field (see, Sagaut, 2003, for a review). The filtering operation of $u(x,t)$ (also called for convenience volume filtering process in the following), for example, is defined on a calculation domain Ω by

$$\overline{u(x,t)} = G \bigstar u = \int_{-\infty}^{t} \int_{\Omega} G(\overline{\Delta}(x,t), x - x', t - t').u(x',t') \, \mathrm{d}x' \, \mathrm{d}t' \tag{24}$$

where G is a formal operator, $\overline{\Delta}$ is the cutoff lengthscale of the filter, and $\Omega \subset \mathscr{R}^3$.

We assume that G commutes with the spatial and time derivation. It is well known that this property is not exactly verified in the inhomogeneous direction of the flows. It would be interesting to verify the order of the error involved in the case of two-phase flows.

On the other hand, the operator G in RANS modeling corresponds to a statistical average of the field (see, e.g., Piquet (1999) for a review). The filtering operation of $u(x,t)$ is expressed as

$$\overline{u(x,t)} = G \bigstar u = \lim_{N \to +\infty} \frac{1}{N} \sum_{p=1}^{N} u_p(x_i, t) \tag{25}$$

where $\{u_p, p = 1, N\}$ represents the value of u for a given pth try of the same flow (i.e. with all temporal or spatial boundary conditions statistically equal).

It is well known that RANS modeling produces a simpler mathematical formulation than LES. Indeed, the properties of the filtering operator are valid for the statistical average and several other properties are specific to the RANS averaging operator. To keep this work as general as possible, the operator will be applied to the set of Eqs. (16) and (17).

The commutation between the derivative and the filter is widely assumed in single-phase LES (see Sagaut, 2003). Let us assume the same for multiphase flows. Such assumption has to be verified, even if, at least theoretically, the commutation error depends more on the topology of the mesh than on the characteristics of the flow (see the works of Dakhoul and Bedford (1986a,b) and Vasilyev et al. (1998), for instance, on non-homogeneous filtering).

Clearly, the filtering of the phase indicator function is of great importance. We set

$$\alpha^k = \overline{\chi^k} \tag{26}$$

It is worth noting that α^k is a "smooth" indicator function and no longer satisfies property (12). That is

$$\alpha^l \alpha^m \neq 0$$

because α varies continuously from 0 to 1.

However, property (11) is always valid, such that

$$\sum_k \alpha^k = 1 \tag{27}$$

The resolved normal vector can be defined as

$$\widehat{n^k} = \begin{cases} -\dfrac{\nabla\alpha^k}{\|\nabla\alpha^k\|} & \text{if } \|\nabla\alpha^k\| \neq 0 \\ 0 & \text{otherwise} \end{cases} \tag{28}$$

A formal definition for the "resolved filtered Dirac function" $\widehat{\delta_i}$ is given as

$$\widehat{\delta_i} = \|\widehat{n^k}\| \tag{29}$$

Furthermore, following Favre et al. (1976), the "phase-weighted" filtering of the variable ϕ^k is defined as

$$\alpha^k\widetilde{\phi^k} = \overline{\chi^k\phi^k} \tag{30}$$

Under this assumption, the filtered set of equations for multiphase flow reads:

(1) Mass:

$$\frac{\partial\alpha^k\widetilde{\rho^k}}{\partial t} + \nabla\cdot(\alpha^k\widetilde{\rho^k u^k}) = \overline{\rho^k(W-u^k)\cdot n^k\delta_i} \tag{31}$$

(2) Momentum:

$$\frac{\partial\alpha^k\widetilde{\rho^k u^k}}{\partial t} + \nabla\cdot(\alpha^k\rho^k\widetilde{u^k\otimes u^k} + \alpha^k\widetilde{p^k}\,\mathrm{Id} - \alpha^k\widetilde{\tau^k}) - \alpha^k\widetilde{\rho^k}g = \overline{(\rho^k u^k\otimes(W-u^k) - p^k\,\mathrm{Id} + \tau^k)\cdot n^k\delta_i} \tag{32}$$

(3) The evolution of the phase indicator function has to be added to these three classical equations:

$$\frac{\partial\alpha^k}{\partial t} = \overline{W\cdot n^k\delta_i} \tag{33}$$

The non-linear terms have to be modeled as none of them can be directly computed. On the left-hand side of the equation, phase-weighted non-linear terms are introduced, while on the right-hand side, we retrieve filtered interfacial terms.

To build a one-fluid filtered formulation, let us define $\overline{\phi}$ as the filtering of the one-fluid variable proposed in Eq. (18):

$$\overline{\phi} = \overline{\sum_k \chi^k\phi^k} \tag{34}$$

Using this definition and summing the evolution equations over all the phases, we obtain

(1) Mass:

$$\frac{\partial\overline{\rho}}{\partial t} + \nabla\cdot(\overline{\rho u}) = \overline{\sum_k(\rho^k(W-u^k)\cdot n^k\delta_i)} \tag{35}$$

(2) Momentum:

$$\frac{\partial\overline{\rho u}}{\partial t} + \nabla\cdot(\overline{\rho u\otimes u} + \overline{p}\,\mathrm{Id} - \overline{\tau}) - \overline{\rho}g = \overline{\sum_k(\rho^k u^k\otimes(W-u^k) - p^k\,\mathrm{Id} + \tau^k)\cdot n^k\delta_i} \tag{36}$$

The quantities arising in the right-hand side of Eqs. (35) and (36) are the overlined counterparts of the jump-condition quantities defined in Eqs. (6) and (7). Expressions (6) and (7) can then be used to replace the right-hand-side quantities of the previous equation.

It is worth noting that it can be more convenient to use as unknown the so-called "Favre average", Favre et al. (1976) (also called in the following mass-weighted filtering) for the velocity field. In this case, a new definition for the filtering of u is employed:

$$\widetilde{u} = \frac{\overline{\rho u}}{\overline{\rho}} \tag{37}$$

The discussion about the choice of the best filtering process is widely tackled in the proceedings of Labourasse et al. (2004), but some complementary issues are presented in the following of this paper. We choose to derive the two formulation (phase-weighted or not), because the use of the phase-weighted average is not always easy when two incompressible phases are considered. In this case, the well-known incompressibility constraint for the filtered field

$$\nabla \cdot \bar{u} = 0 \tag{38}$$

is always valid, spurious terms appears when using the mass-weighted average, and this constraint becomes

$$\nabla \cdot \tilde{u} = \frac{[\rho]}{\bar{\rho}}(\overline{u \cdot n} - \tilde{u} \cdot \hat{n}) \tag{39}$$

where $[\rho]$ accounts for the jump of the density across the interface. The solving of Eq. (39) is far more complicated, and one can prefer using the non-weighted filtering process, unless the additional term arising in the momentum equation.

3. Closures

The closure of the system is very complicated and makes the thematic of the filtering for multiphase flows very rich. The closure terms can be classified into three categories as follows:

(i) The "classical" subgrid terms, which account for the effects of subgrid scale correlations on the resolved flow, and which arise in the equations from the non-linearities. They are common to single-phase turbulence studies, and the large amount of modeling work already done on this field (see, Sagaut, 2003, for a review) can be partly used. Nevertheless, the hierarchical classification in magnitude of the subgrid scale contributions proposed by Vreman et al. (1995) and Vreman (1995) (for the momentum equations all subgrid terms are negligible but the one coming from $\overline{\rho u \otimes u}$) may not be suitable near the interface. However, all new modeling must tend to classical modeling in the single-phase areas.

(ii) The pure interfacial subgrid terms, which take into account the subgrid contribution of the interface characteristics to the flow evolution. In the set of Eqs. (35) and (36), these terms appear in the right-hand side and can be replaced using the jump conditions given by Eqs. (6) and (7).

(iii) The subgrid error committed by using thermodynamical and physical laws to represent a mixed phase volume of fluid. This problem has been partly tackled by Duquennoy et al. (1999) and Mathieu et al. (2003) (in particular, with a great contribution to the modeling of the contact lines), but remains mainly untouched.In the present study, isothermal flows are only considered as a preliminary stage. Therefore, the influence of the first two subgrid terms (i) and (ii) can be evaluated.

In this work we will focus on the one-fluid model, and all the non-linear terms of the system of equations (35) and (36) will be written using the resolved variables

$$\tau_{\phi\psi} = \overline{\phi\psi} - \overline{\phi}\,\overline{\psi} \tag{40}$$

where $\tau_{\phi\psi}$ is the subgrid contribution of non-linearity to the filtered evolution equations, and has to be closed using the resolved quantities. From now, the subscripts l and r are respectively related to left and right-hand-side terms in Eqs. (35) and (36). Moreover, when this is necessary, the subscript f is added when using the mass-weighted filtering process for Eqs. (60) and (61).

Considering the left-hand-side of Eqs. (35) and (36), the following terms have to be modeled:

- Mass:

$$\tau_{l\rho u} = \overline{\rho u} - \overline{\rho}\,\bar{u} \tag{41}$$

- Momentum:

$$\tau_{l\rho uu} = \overline{\rho u \otimes u} - \overline{\rho}\tilde{u} \otimes \tilde{u} \tag{42}$$

$$\tau_{l\mu S} = \overline{\tau} - \overline{\mu}\overline{S_D} \tag{43}$$

The use of the filtering variable $\tilde{u}$ allows us to avoid the subgrid scale term into the time derivative. The new non-linear terms that have to be taken into account owing to the non-linear terms in left-hand-side of the equation are:

- Mass: No more subgrid terms appear in the right-hand-side of this equation.
- Momentum:

$$\tau_{fl\rho uu} = \overline{\rho u \otimes u} - \overline{\rho}\tilde{u} \otimes \tilde{u} \tag{44}$$

$$\tau_{fl\mu S} = \overline{\tau} - \overline{\mu}\overline{S_D} \tag{45}$$

In the right-hand-side of the equation, the expression of the subgrid terms does not change.
The following observations should be noted:

- These subgrid terms are formally not different from those that can be found in filtering a single-phase flow. However, the concluding remarks of Vreman et al. (1995) and Vreman (1995) on the order of magnitude of each of them cannot be used in the case of multiphase flows. Indeed, the term $\tau_{l\mu S}$, for instance, is found negligible in the work of Vreman because of the low variation of μ. However, for multiphase flows, μ can vary sharply through the interface, since it depends on the phases that are considered.
- It is interesting to decompose terms (41)–(43) to make the different phases appear. For instance, let us decompose $\tau_{l\rho u}$ into k phases:

$$\begin{aligned}\tau_{l\rho u} &= \sum_k (\overline{\chi^k \rho^k u^k}) - \sum_k (\overline{\chi^k \rho^k}) \sum_k (\overline{\chi^k u^k}) = \sum_k (\overline{\chi^k \rho^k u^k} - \overline{\chi^k \rho^k \chi^k u^k}) - \sum_{k \neq l} (\alpha^k \widetilde{\rho^k} \alpha^l \widetilde{u^l}) \\ &= \sum_k \tau^k_{l\rho} - \sum_{k \neq l} (\alpha^k \widetilde{\rho^k} \alpha^l \widetilde{u^l})\end{aligned} \tag{46}$$

The first term on the right-hand side of Eq. (46) is the sum of the classical subgrid terms that exist in each single-phase flow. The second term is a sum of cross terms, which is a peculiar feature of multiphase flows.
- The time derivatives of the subgrid terms $\tau_{l\rho}$ appear in the momentum equation. This system is then difficult to solve directly.
- The use of $\overline{\mu}$, for instance, makes difficult the closure of the equation by the classical thermodynamic laws. It may be more convenient to write for example the resolved dynamic viscosity $\widehat{\mu} = \mu(\overline{T})$.

For the right-hand side of the equations, two strategies can be used. The first one consists in a direct filtering of the system of equations (35) and (36). This will lead to a system in which all phase quantities remain on the right-hand side. The second possibility is to replace the right-hand side of the system of equations (35) and (36) by the filtered quantities coming from the jump conditions (6) and (7).

The first strategy leads to the following subgrid scale terms[4]:

(1) Mass:

$$\tau^k_{r\rho} = \overline{\rho^k (W - u^k) \cdot n^k \delta_i} - \alpha^k \widetilde{\rho^k} \alpha^k (\widetilde{W} - \widetilde{u^k}) \cdot \widehat{n^k} \tag{47}$$

(2) Momentum:

$$\tau^k_{ruu} = \overline{(\rho^k u^k \otimes (W - u^k) - p^k \,\mathrm{Id} + \tau^k) \cdot n^k \delta_i} - (\alpha^k \widetilde{\rho^k} \alpha^k \widetilde{u^k} \alpha^k (\widetilde{W} - \widetilde{u^k}) + \alpha^k \widetilde{p^k}\,\mathrm{Id} + 2\alpha^k \widetilde{\mu^k} \alpha^k \widetilde{S^k_D}) \cdot \widehat{n^k} \tag{48}$$

[4] For the terms appearing in the right-hand side of Eqs. (6) and (7), the notation (40) is no more convenient and is not respected.

(3) Phase advection:

$$\tau^k_{r\chi} = \overline{W \cdot n^k \delta_i} - \widetilde{W} \cdot \widehat{n^k} \tag{49}$$

These two modeling stages lead to the following set of equations:

(1) Mass:

$$\frac{\partial \overline{\rho}}{\partial t} + \nabla \cdot (\overline{\rho}\bar{u} + \tau_{l\rho u}) = \sum_k (\alpha^k \widetilde{\rho^k} \alpha^k (\widetilde{W} - \widetilde{u^k}) \cdot \widehat{n^k}) + \sum_k \tau^k_{r\rho} \tag{50}$$

(2) Momentum:

$$\begin{aligned} &\frac{\partial (\overline{\rho}\bar{u} + \tau_{l\rho u})}{\partial t} + \nabla \cdot (\overline{\rho}\bar{u} \otimes \bar{u} + \bar{p}\,\mathrm{Id} - \overline{\mu S_D} + \tau_{l\rho uu} + \tau_{l\mu S}) - \overline{\rho} g \\ &\quad = \sum_k ((\alpha^k \widetilde{\rho^k} \alpha^k \widetilde{u^k} \otimes \alpha^k (\widetilde{W} - \widetilde{u^k}) + \alpha^k \widetilde{p^k}\,\mathrm{Id} - \alpha^k \widetilde{\mu^k} \alpha^k \widetilde{S^k_D}) \cdot \widehat{n^k}) + \sum_k \tau^k_{ruu} \end{aligned} \tag{51}$$

(3) Phase indicator advection:

$$\sum_k (\widetilde{W} \cdot \widehat{n^k}) + \sum_k \tau^k_{r\chi} = 0 \tag{52}$$

In Eqs. (50) and (51), the first term on the right-hand side corresponds to the approximate jump condition, using the filtered variables (see the left-hand side of Eqs. (6) and (7)). As a consequence, the closure of this system requires: (i) the closure of all the subgrid scale terms and (ii) an approximate jump condition through the interface.

The second strategy is to use the exact jump conditions given by Eqs. (6) and (7) to derive a new system of filtered equations. Note that the commutation error between the filter and the surface derivatives cannot be generally assumed to be zero. The generalized surface gradient and divergence are then defined as follows:

$$\nabla_s \varphi = (\mathrm{Id} - n \otimes n) \cdot \nabla \varphi \Longleftrightarrow \widehat{\nabla_s} \varphi = (\mathrm{Id} - \hat{n} \otimes \hat{n}) \cdot \nabla \varphi \tag{53}$$

$$\nabla_s \cdot \psi = (\mathrm{Id} - n \otimes n) : \nabla \psi \Longleftrightarrow \widehat{\nabla_s} \cdot \psi = (\mathrm{Id} - \hat{n} \otimes \hat{n}) : \nabla \psi \tag{54}$$

Then, the error committed in commuting the filter and the surface derivative will introduce new subgrid scale error terms that have to be calculated.

In this case, the right-hand-side subgrid contributions are:

(1) Mass:

$$\tau_{r\rho} = 0 \tag{55}$$

No contribution appears from the right-hand side for the mass conservation equation, in this case.

(2) Momentum:

$$\tau_{rnn} = -\overline{\sigma n \nabla_s \cdot n \delta_i} + \overline{\sigma} \hat{n} \widehat{\nabla_s} \cdot \hat{n} \tag{56}$$

$$\tau_{r\sigma} = \overline{\nabla_s \sigma} - \widehat{\nabla_s} \overline{\sigma} \tag{57}$$

This second strategy leads to a simpler set of equations

(1) Mass:

$$\frac{\partial \overline{\rho}}{\partial t} + \nabla \cdot (\overline{\rho}\bar{u} + \tau_{l\rho u}) = 0 \tag{58}$$

(2) Momentum:

$$\frac{\partial(\overline{\rho}\bar{u}+\tau_{l\rho u})}{\partial t}+\nabla\cdot(\overline{\rho}\bar{u}\otimes\bar{u}+\bar{p}\,\mathrm{Id}-\overline{\mu S_D}+\tau_{l\rho uu}+\tau_{l\mu S})-\overline{\rho}g=\overline{\sigma}\hat{n}\widehat{\nabla_s}\hat{n}-\widehat{\nabla_s}\overline{\sigma}+\tau_{rnn}+\tau_{r\sigma} \tag{59}$$

or in using the mass-weighted filtered variable $\tilde{u}$:

(1) Mass:

$$\frac{\partial\overline{\rho}}{\partial t}+\nabla\cdot(\overline{\rho}\tilde{u})=0 \tag{60}$$

(2) Momentum:

$$\frac{\partial\overline{\rho}\tilde{u}}{\partial t}+\nabla\cdot(\overline{\rho}\tilde{u}\otimes\tilde{u}+\bar{p}\,\mathrm{Id}-\overline{\mu S_D}+\tau_{fl\rho uu}+\tau_{l\mu S})-\overline{\rho}g=\overline{\sigma}\hat{n}\widehat{\nabla_s}\hat{n}-\widehat{\nabla_s}\overline{\sigma}+\tau_{rnn}+\tau_{r\sigma} \tag{61}$$

This second formulation, more tractable, will be employed for performing the following applications.

4. Numerical methods

One of the main difficulties of this work consists in obtaining precise DNS results. Indeed, the numerical method has to satisfy the mesh convergence condition: when the mesh resolution increases, the result of the simulation has to tend towards the exact solution. Therefore, most of the numerical methods employed for two-phase flow simulation do not fulfill this condition when surface tension is taken into account (see, e.g., Scardovelli, 1999). In particular, the description of the interfacial area is often not precise enough to give satisfactory results (see for instance Lebaigue et al. (1998) for an introduction to the different methods available). The Eulerian methods generally involve an approximate reconstruction of the interface, which leads to an inexact modeling of the surface tension contribution. The original Front-Tracking method suffers from the same problem since the interfaces are smeared (Hirt and Nichols, 1981; Juric and Tryggvason, 1998). These approximations lead to the growth of purely rotational structures called parasitic currents, which do not decrease as the mesh size becomes smaller (Brackbill et al., 1992). The Arbitrary Lagrangian Eulerian methods (ALE) (see, Welch, 1995, for instance) allows these spurious currents to be avoided. However, this technique is difficult to implement and still remains numerically too expensive to be employed to simulate complex phenomena (boiling, mass transfer, break-up,...). Even if the issue of spurious currents is not discussed, the Eulerian level set/vortex sheet method proposed by Herrmann (2005) is very promising for the study of two-phase flow in turbulent environment, specifically for atomization process. Some new formulations for the VOF method (Gueyffier et al., 1999; Vincent et al., 2004b) and for the Front-Tracking method (Juric and Tryggvason, 1998; Mathieu et al., 2003) have been proposed in order to prevent spurious currents.

In this work, two test cases are considered (see following section). In the problem of the two counter-rotating vortices impacting a bubble, the Front-Tracking method of Mathieu et al. (2003), implemented in Trio_U (see Calvin et al., 2002), will be used. This method is a dedicated "sharp interface" version of the Front-Tracking approach, which does not resort to usual explicit smoothing function of the interfaces. Since the interfaces are not smeared, the method can accurately capture the turbulent transfer between the two phases. It was assessed on many application tests comparing with analytical solutions (Mathieu, 2003). This original method benefits from the VOF method for the calculation of the indicator function. Nevertheless, the interfaces are explicitly described using a Lagrangian mesh, moving on an Eulerian mesh for the flux calculation as for the classical Front-Tracking method. Each elementary surface (respectively segment) describing the interface in 3D (respectively 2D) is designed with 3 (respectively 2) points. The displacement of these points follows the law

$$\frac{\mathrm{d}x}{\mathrm{d}t}=W \tag{62}$$

which can be expressed using Eq. (6), as

$$W \sum_k \rho^k = \sum_k n^k (\rho^k u^k \cdot n^k - \dot{m}^k) \tag{63}$$

An original discretization of the surface tension and gravity forces is used, in order to obtain an irrotational discrete contribution of the sum of these terms in the momentum equation, leading to zero parasitic current. An explicit Euler scheme for the time integration is used. A QUICK third order method is implemented for the spatial discretization of the convection terms. The diffusion terms are discretized using a second order centered scheme. The pressure is computed using a Cholesky method. A complete description of the numerical code and the validation can be found in Mathieu et al. (2003) and Mathieu (2003).

In the second test case dedicated to the phase inversion in a closed box, the motion equations are approximated by an implicit Finite-Volume method on a staggered mesh while an adaptative augmented Lagrangian technique is investigated to solve the coupling between pressure and velocity in the equations of motion (Vincent et al., 2004b). The spatial discretization of these Navier–Stokes equations is achieved through a second-order Euler scheme, or GEAR scheme, on the time derivatives while a second order Hybrid Centered-Upwind scheme is devoted to the non-linear convective terms and a second order centered scheme is chosen for the approximation of the viscous and the augmented Lagrangian terms. An iterative BiCGSTAB II (Bi-Conjugate Gradient Stabilized) solver, preconditioned under a Modified and Incomplete LU (MILU) algorithm, is implemented to tackle with the linear system resulting from the previous implicit discretization. All the references concerning the numerical methods can be found in Vincent and Caltagirone (2000).

The numerical simulations are run with a Piecewise Linear Interface Construction (VOF-PLIC) method of Youngs (1982) using the Continuum Surface Force (CSF) method (Brackbill et al., 1992) for the treatment of the surface tension.

Note that, with this numerical method, the evolution Eq. (33) for the void fraction replaces Eq. (63) for the displacement of the interface in Front-Tracking. Without phase change, this equation degenerates into:

$$\frac{\partial \alpha^k}{\partial t} + u \cdot \nabla \alpha^k = 0 \tag{64}$$

In filtering or averaging Eqs. (63) and (64), some specific subgrid terms appear, depending on the Lagrangian or Eulerian characteristic of each approach. These terms depends on the numerical method employed and are not considered in the present work.

5. Numerical experiments

The two selected cases are now studied, in order to estimate the relative weights of the different subgrid scale terms of two-phase flow equations. It consists in a 2D DNS of elementary calculation cases that are representative of the turbulent phenomena. The 2D DNS takes advantage of the relatively low cost of the calculations to make it possible to perform a parametrical analysis of the relative magnitude of the subgrid scale contributions without loss of pertinence.

5.1. General physical assumptions

The following assumptions have been adopted (see for example Drew, 1983; Magnaudet, 1997) for all the test cases presented afterwards:

(1) Only two phases are considered: this assumption does not formally simplify the equations. However, the meaning of the jump conditions is much clearer with only two phases.
(2) The density is constant in each of the two phases: this condition does not really simplify the one-fluid formulation, since $\rho = \sum_k \chi^k \rho^k$ varies in space and time. Nevertheless, when added to the fourth assumption, it allows the energy equation to be uncoupled from the rest of the system. Therefore, the energy equation is not solved in the following test cases.

(3) There is no mass transfer between the phases: this condition translates mathematically into $\dot{m}^k = 0$ which is equivalent to $W \cdot n^k = u^k \cdot n^k$. It considerably simplifies the system of equations (50)–(52). However, no further simplification of system (58) and (59) is expected.
(4) The situations of interest are isothermal and without any chemical reaction: this condition allows μ for each phase and σ to be set as constants, since assuming respectively that the Sutherland and the Gibbs–Duhem laws are valid, μ depends only on the temperature and σ depends on the temperature and the chemical potential.
(5) There is no sliding between phases: the introduction of this assumption simplifies the one-fluid model assuming the average velocity gradients to be equal at a given point and in each phase. Thanks to this condition, we obtain the commutativity property between the filtering and the gradient operator. Thus, interfacial subgrid terms can be neglected.
(6) The fluids are non-miscible: this assumption implies no mass diffusion. At a subgrid scale the diffusion is only a consequence of the numerical scheme's artifacts. This explains that no equation considering any specific material property is solved but a kinematic relation bounding the interface velocity and the local volume fraction, the advection Eq. (33). The definition of volume fraction dedicated to each phase also allows an interface to be defined by $\alpha_k = 0.5$.

The phases that are considered in this work are air, water, viscous water and oil. Table 1 recalls their physical parameters.

Classical values of the surface tension at room pressure and temperature conditions are used for test case 1 (water–air, $\sigma = 0.07\ \mathrm{N\ m^{-1}}$) and test case 2 (viscous water–oil, $\sigma = 0.045\ \mathrm{N\ m^{-1}}$).

Two academic calculation cases are now presented, which are relevant of the specific problems of interface/turbulence interaction. The first case accounts for the simpler model for turbulent structures interacting with a bubble, and the second test case for *interfacial turbulence*, i.e. high Weber number flow producing subgrid inclusions. These two cases are complementary and are representative of a wide range of problems going from bubbly channels to breaking waves.

5.2. Test case 1: Impact of two counter-rotating vortices with a bubble

5.2.1. Definition

The objective of this first test case is to observe the effects of turbulence on the interface of a 2D bubble, and the reciprocal influence of the interface on the behavior of the turbulence. For this case, there is no gravity effect and the turbulence is idealized in the form of isentropic vortices. In order to keep the bubble motionless without using any non-physical forcing term, two-counter-rotative vortices are used, interacting with each other to go down to the bubble. This case is very relevant, especially for bubbly flows, because LES modeling is useful when the smallest turbulent scales are much smaller than the interfacial scales. In this case, even if the bubble interface is accurately discretized, active turbulent scales remain subgrid and have to be modeled. The most energetic under-resolved coherent structures have then a size slightly lower than the one of the bubble. These coherent structures are unpredictable vortices (see for instance the book of Batchelor (1974)). For three-dimensional cases (and for barotropic fluid), the evolution of these vortices is mainly driven by two phenomena: (i) the stretching of the vortex by the velocity field and (ii) the diffusion of the vortex thanks to the viscosity. It is worth noting that the first phenomenon does not exist for two-dimensional flow. Nevertheless,

Table 1
Physical parameters for all the calculations

	ρ (kg m^{-3})	μ (kg m^{-1} s^{-1})	ν (m^2 s^{-1})
Air	1.3	2×10^{-5}	1.54×10^{-5}
Water	1000	10^{-3}	10^{-6}
Ratio air/water	1.3×10^{-3}	2×10^{-2}	15.4
Oil	900	10^{-1}	1.1×10^{-4}
Viscous water	1000	5×10^{-3}	5×10^{-6}
Ratio oil/viscous water	0.9	20	22

this is expected not to be crucial for our purpose, that is sort the magnitude of the subgrid scale terms. That is why the 2D interaction of the bubble with a vortex seems to us to be the more relevant test case for this work, allowing a parametrical study thanks to the relatively low cost of the simulation. Moreover, in the case of bubbly flow, a wide part of the turbulent effects is produced by the wakes of the bubbles themselves, which are of size slightly lower than the bubbles.

It is worth noting that this test case essentially mimics the integral scale of turbulence. To complete this case, a study of the behavior of inclusions in a homogeneous isotropic turbulence would be of interest, accounting for the Taylor microscale of the turbulence/interface interaction, but this is beyond the scope of this paper.

Each vortex is initialized with the following equation:

$$V_v = \begin{pmatrix} u_v \\ v_v \end{pmatrix} = \frac{w}{2\pi} e^{0.5\left(1-\left(\frac{r}{R_v}\right)^2\right)} \begin{pmatrix} -y + y_v \\ x - x_v \end{pmatrix} \tag{65}$$

where $r^2 = (x - x_v)^2 + (y - y_v)^2$ and w, R_v, x_v and y_v correspond respectively to the angular velocity, the radius and the coordinates of the center of the vortex.

The parameters used for the initialization of the study are presented in Fig. 1. For all the test cases, a 200×216 mesh is then used leading to a mesh size of 3×10^{-5} m.

This very simple configuration allows us to reproduce a wide range of interface–turbulence interactions in modifying the parameters of the simulations. These parameters are summarized in Table 5.

5.2.2. Macroscopic behavior

The case (N0) accounts for a slightly disturbed interface. In the approximation of small disturbances, analytical results are available, which validates the calculation. The time-evolution of the isovalues of the vorticity is plotted in Fig. 2. It can be seen that the shape of the interface is hardly deformed by the impact of the vortices.

For the (Solid) case, the phase inside the bubble is characterized by a very high density and a very high viscosity with respect to those of the liquid, and a very high surface tension. So, the bubble behaves like a solid cylinder. The time-evolution of the isovalues of the vorticity is plotted in Fig. 3.

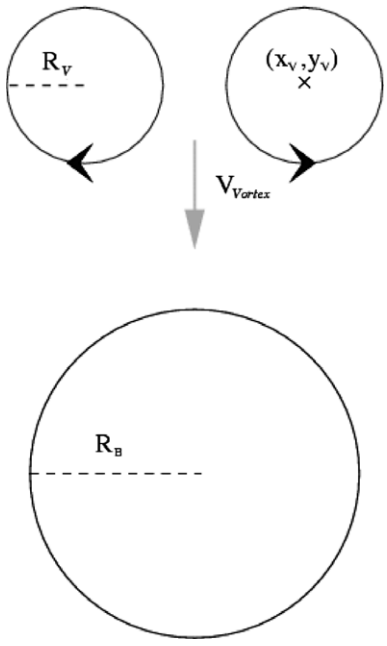

Fig. 1. Mean parameters used in the bubble/turbulence interaction test case.

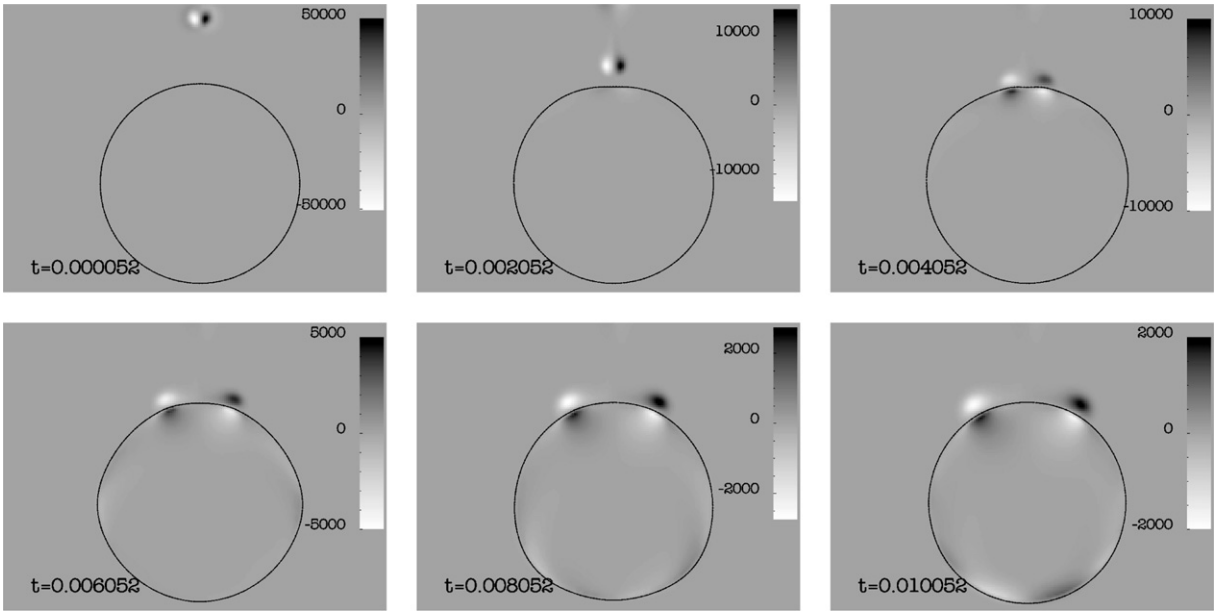

Fig. 2. Time evolution of the isovalues of the vorticity and of the position of the interface.

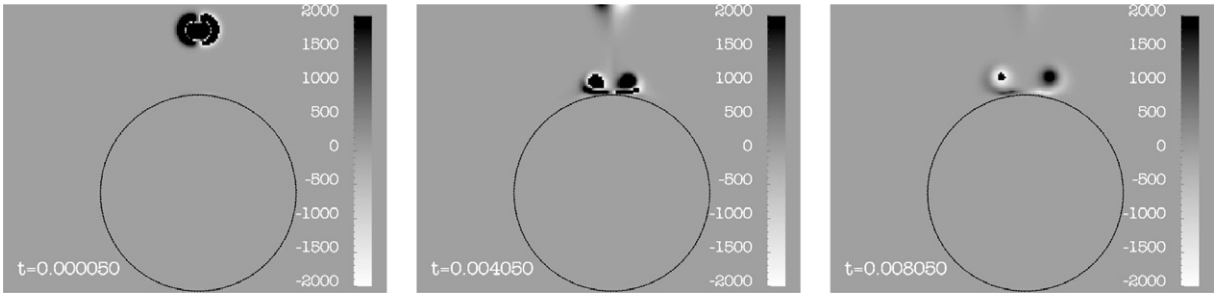

Fig. 3. Time evolution of the isovalues of the vorticity and of the position of the interface (Solid case).

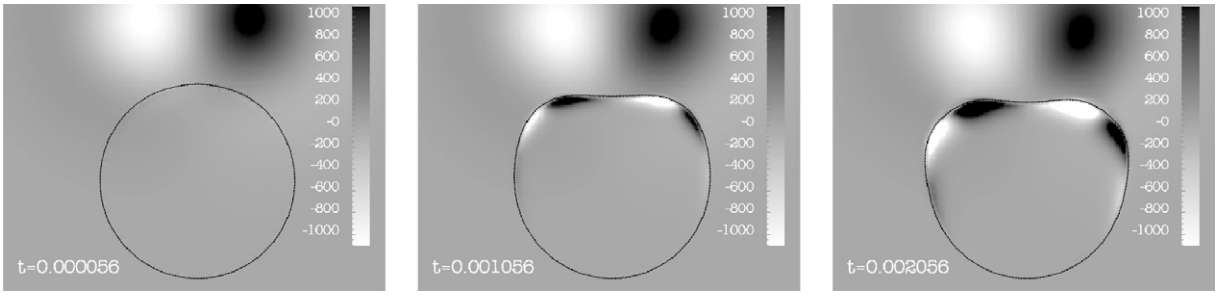

Fig. 4. Time evolution of the isovalues of the vorticity and of the position of the interface (N1 case).

For the (N1) case, the bubble is much more distorted. The time-evolution of the isovalues of the vorticity is plotted in Fig. 4.

For the three cases, the maximum of velocity is obtained for $r = R_v$ and is equal to: $V_M = w/(2\pi)$. Each vortex moves downward with a velocity determined by that of the other vortex, called V_{vortex}.

It can be noted that the Kolmogorov length scale associated with this problem can easily be approximated by

$$\eta(t) \approx \nu^{1/2} \|\omega\|_{\max}(t)^{-1/2} \tag{66}$$

where $\omega = \nabla \times u$ is the vorticity vector. Indeed, $\eta = \varepsilon^{-1/4}\nu^{3/4}$ and $\varepsilon \approx \nu \nabla u : \nabla u \approx \nu \|\omega\|^2_{\max}$.

For the (N0) case, the Kolmogorov scale η is initially three times smaller than the mesh size. This is not a problem since the vorticity quickly decreases and η is largely greater than the mesh size when the vortices interact with the bubble. Indeed, it can be demonstrated that the enstrophy freely decreases as the square of time (Lesieur, 1990 for instance).

Here, the enstrophy $D = \langle (\nabla \times u)^2 \rangle$ is equal to the square of the instant vorticity (at least before the impact of the vortices with the bubble). The time-evolution of the maximal vorticity is given in Fig. 5 and fits correctly the $1/t$ law.

To validate the numerical methods, mesh convergence tests and comparison with theoretical results have been undertaken (Lemonnier and Jamet, 2004).

The behavior of the bubble and in particular the correct estimate of the oscillatory frequencies for the test (N0) allows us to validate the calculation of the capillarity forces (see Fig. 6 and Table 2). This figure shows

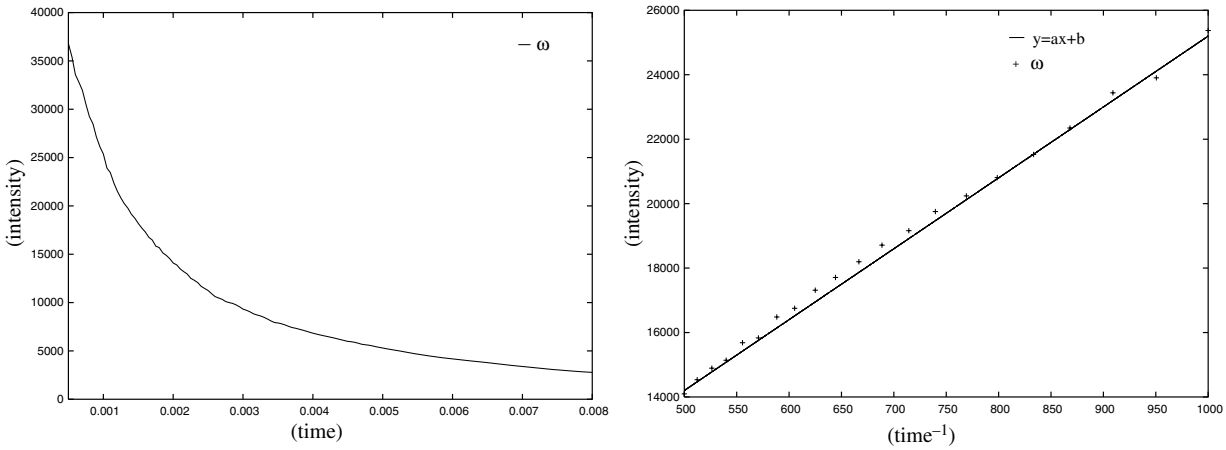

Fig. 5. Evolution of the maximal vorticity – left: $w = f(t)$, right $w = f(1/t)$.

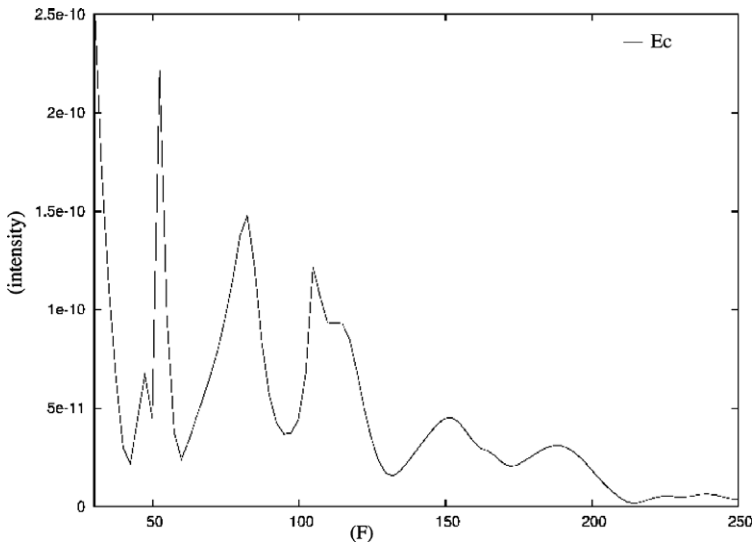

Fig. 6. Kinetic energy spectrum.

Table 2
Comparison between the eigen modes of the bubble and oscillatory behavior of E_c

p_b Eigen mode	F_b Eigen frequency (Hz)	F_e Corresponding energy peak frequency (Hz)	$F_e - F_b$ (Hz)	E_f Theoretical maximum error (Hz)
3	52	52.2	0.2	2.7
4	82	82.5	0.5	6.8
5	105	116.6	11.6	13.6
6	152	154.3	2.3	23.8
7	187	195.1	8.1	38.1

the spectral distribution of kinetic energy, computed through a Fourier transform. The scales containing the most energy do not correspond with the vorticity time scale, but with the eigen mode of mechanical bubble energy.

Indeed, an analytical calculation of the oscillations of a bubble in a 2D potential fluid (Lamb, 1993), gives us the theoretical eigen frequency of an inclusion for a bubble lightly deformed (as it is the case for the test (N0)):

$$\omega_p^2 = \frac{p(p^2-1)\sigma}{\sum_k \rho^k R^3} \tag{67}$$

Table 2 shows a comparison between the frequencies obtained using this analytical calculation and the high energetic scale presented in Fig. 6. A simple theoretical evaluation of the maximal error that can arise when proceeding to the Fourier transform of the energy signal can be obtained using the formula

$$E_f \approx F(F\delta T + \mathcal{O}(F\delta T)) \tag{68}$$

where F is the targeted frequency, and δT is the sampling time.

This good agreement between these two frequencies implies that the "turbulent" high frequency kinetic energy is transformed into low frequency surface energy. It also attests of the quality of the simulation.

This interesting feature can be attributed to the term $\sigma n \cdot W\nabla_s \cdot n$. Moreover, the interface seems to enforce the frequencies of this transformation to its own eigen modes. This means that the time scale

$$t_p = 2\pi\sqrt{\frac{\sum_k \rho^k R^3}{p(p^2-1)\sigma}} \tag{69}$$

seems to be the most important new one for modeling subgrid scale turbulent induced phenomena, since energetic effects are often privileged in turbulence.

It is worth noting that this oscillatory behavior can alter the motion of the bubble, contributing in making it hard to predict. Our experience show us that capturing the right motion of the bubble must then require a modeling for the subgrid term τ_{rnn} even if its weight is weak in the momentum equation.

To validate the other test cases, no analytical solutions are available. We have then performed mesh convergence tests to validate the calculations. The convergence test for the case (N1) is presented in Fig. 7.

5.3. Test case 2: Phase inversion in a closed box

5.3.1. Definition

A complex phase inversion problem in a closed box is considered with highly deformed interface (high Weber number). This test case is complementary to the previous one, studying a turbulent regime very peculiar to two-phase flows, which can be called *interfacial turbulence*. A square oil inclusion of height $L = 0.5$ m is initially located in the left corner of a square cavity full of viscous water of length $H = 1$ m. Gravity and surface tension effects are taken into account. As $L = H/2$, the equilibrium heights of the oil and viscous water layers after phase inversion are respectively $H/4$ and $3H/4$ in two dimensions. Both phases are initially at rest and no slip boundary conditions are imposed on the walls of the closed cavity.

The physical characteristics of oil and viscous water are those detailed in Table 1. The surface tension σ is 0.045 N m^{-1}. Based on the characteristic velocity $u_0 = \sqrt{gH} = 0.99$ m s^{-1}, where $g = 9.81$ m s^{-2} is gravity, the

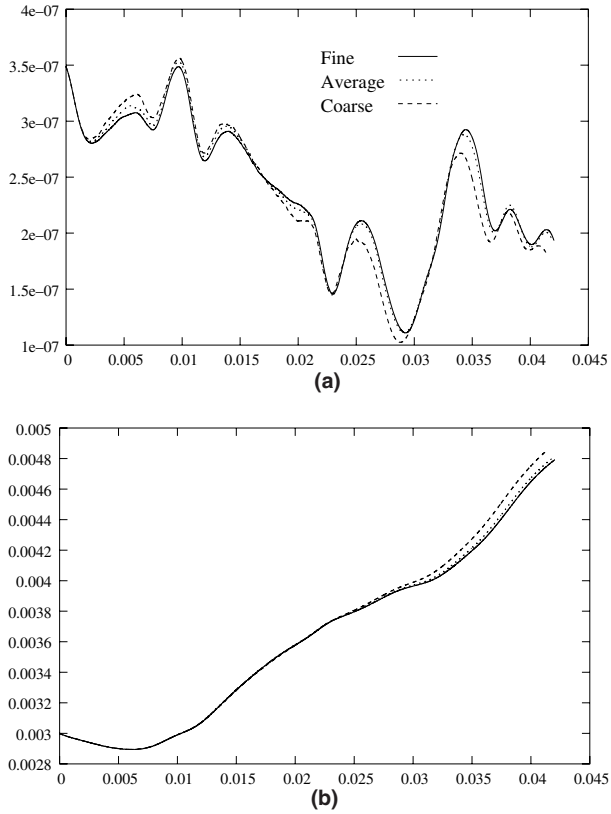

Fig. 7. Mesh convergency (time evolution): (a) kinetic energy and (b) vertical coordinate.

characteristic dimensionless numbers of the problem are the Weber and the Reynolds numbers (in oil and viscous water respectively) defined by

- $We = \frac{(\rho_w - \rho_0) u_0^2 L}{\sigma} = 1089$,
- $Re_w = \frac{\rho_w u_0 L}{\mu_w} = 99000$,
- $Re_0 = \frac{\rho_0 u_0 L}{\mu_0} = 1455$.

A convergence analysis has been performed to evaluate the effect of the mesh grid size on the physical solution as depicted in Fig. 9. Regular Cartesian 128×128, 256×256 and 512×512 mesh grids have been considered. The kinetic and potential energies and the volume ratio are the three physical characteristics studied. They have been respectively non-dimensionalized by the maximum magnitude of the kinetic energy reached during the calculation on the 512×512 grid, $\int_\Omega \rho g z \, dv$ and the total volume of the cavity. Whatever the characteristic investigated, the physical solution appears to converge as the mesh grid size gets finer. As a consequence, this numerical exercise is a DNS as no explicit turbulence model is considered and the physical solution has converged. Nevertheless, depending on the numerical properties of the VOF methods, the smaller interface structures are of the order of Δx. Thus, refining the mesh grid will induce an increase of small droplets generation, this, in turn, having no influence on the general solution.

The flow induced by the action of the buoyancy force due to oil inclusion in a cavity full of viscous water is studied. Since the density difference effect is counteracted by the viscous and surface tension forces, an unsteady turbulent two-phase flow develops. This leads to strong interface shearing and stretching accompanied with drop extraction and collapsing. The interest of this test case is the simplicity of its initial condition and the complexity of the interface structures generated in terms of strong deformations, shear instabilities and droplet coalescence (see Vincent et al., 2004a). In this regard, this case study is aimed at testing the ability of the numerical method to simulate turbulent two-phase flows with large and dynamic interface deforma-

tions. Due to the complexity of the flow, the detailed structure cannot be analyzed and compared to any reference solution. Moreover, the detailed time evolution of the transient phase may be not completely resolved at each time step due to the fine structure of the eddies that are produced. The second asset of the problem is the existence of a theoretical solution for sufficiently long times concerning the exact position of the interface, which corresponds to a horizontal oil layer in the top part of the cavity and a horizontal viscous water layer in the bottom part of the square box. At equilibrium, the two fluids are separated by a horizontal interface and its position only depends on the initial volumes of the fluids. In this regard, this test case is particularly relevant to test the ability of a numerical code to conserve mass and volume even for very large and complex interface deformations. To finish with, the independence of the steady solution of the phase inversion problem on the physical parameters such as density, viscosity or surface tension allows various numerical methods and physical configurations to be dealt with.

5.3.2. Macroscopic behavior

Fig. 8 illustrates the temporal evolution of the two phases. The very unstable initial configuration induces the development of Rayleigh–Taylor-like instabilities. According to the theory of the instabilities, the critical value of the wavelength below which the surface tension damps the instability of the structures is given by Chandrasekhar (1981)

$$\lambda_c = 2\pi\left[\frac{\sigma}{g(\rho_w - \rho_0)}\right]^{1/2} = 0.04m \tag{70}$$

This means that even very small drops remain unstable in this flow, which leads to a great shear (4th sub-figure 4.5 s to 7th sub-figure 22.25 s, of Fig. 8). The theoretical terminal velocity of an inclusion of oil in the viscous water is proportional to $\frac{\rho_w-\rho_0}{\rho_w}$ Harper (1972), and is then quite small. This partly explains why the steady state is very long to reach. In addition, as already explained in Section 5.3.1, a high number of droplets are generated (Fig. 8).

Figs. 9 and 13 represent the temporal evolution of some macroscopic quantities for the two phases while the enstrophy is given in Fig. 10. The initial configuration of the two phases is highly unstable, and the capillarity term acts as a source of enstrophy. Thus, both the total enstrophy (that is the square of the vorticity integrated over the whole domain) and kinetic energy increase at the beginning of the calculation as the oil inclusion starts to migrate. The maximum magnitudes in both fluids are reached at a time around 5 s, which corresponds to the highest shear rate of the two-phase flow. As depicted in Fig. 8, the oil phase remains in one major piece at $t = 4.5$ s and from this time, it stretches and breaks up in many small droplets ($t = 6.25$ s). This process corresponds to a dramatically decrease of the kinetic energy and enstrophy until around $t \simeq 20$ s. Indeed, the major part of the oil phase has reached the top of the box and an oscillatory momentum is established in the cavity, more and more damped by the oil layer. This dynamics can be clearly seen in Fig. 13 where the potential energy and the volume ratio evolutions are presented. It can be observed that around $t \simeq 20$ s, nearly all the oil phase is in the upper quarter part of the domain whereas the water phase is contained in the rest of the box. The temporal evolution of the potential energy clearly indicates that both phases reach a state of equilibrium at the end of the inversion process.

6. *A priori* comparison of the order of magnitude of the different subgrid-scale terms

In this section, some *a priori* tests are undertaken, in order to sort the different subgrid scale terms of the two-phase flow equations according to their relative importance. The main idea is to explicitly filter the equations to examine the relative quantitative impact of the different non-linear terms in the equations in the under-resolved case.

The top-hat filter is used following the idea of Vreman et al. (1995) in order to explicitly obtain the magnitude of the error terms $\frac{\partial \tau_{l\rho u}}{\partial t}$, $\nabla \cdot \tau_{l\rho uu}$, $\nabla \cdot \tau_{l\mu S}$ and τ_{rnn}. The kernel of this filter is given by

$$G(z) = \begin{cases} \frac{1}{\Delta X \Delta Y} & \text{if } z \in [-\Delta X/2, \Delta X/2] \times [-\Delta Y/2, \Delta Y/2] \\ 0 & \text{otherwise} \end{cases} \tag{71}$$

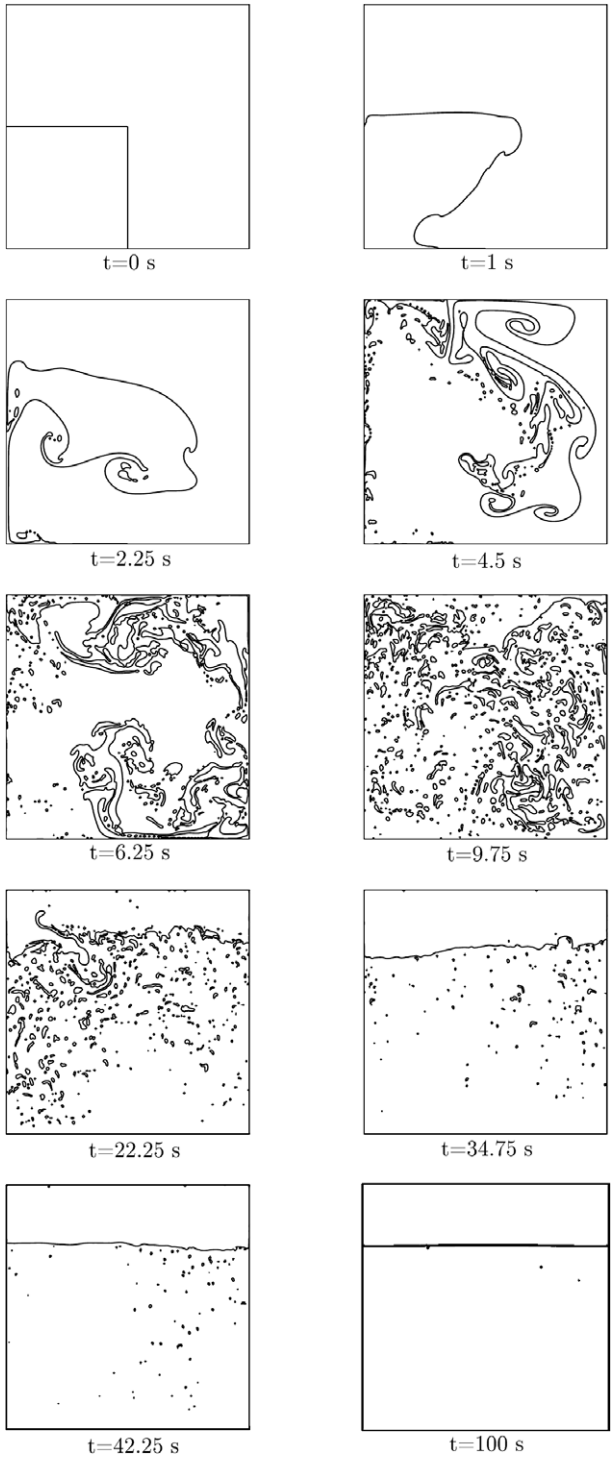

Fig. 8. Quasi-direct numerical simulation of the phase inversion problem in two-dimensions for oil and viscous water. With $\Delta x = 3.91 \times 10^{-3}$ m, the results show the interface profiles. The computation is stopped after thousands of iterations. For longer times, a steady state with two horizontal layers should be obtained.

In the following, the field is filtered over the DNS fine mesh. For a given variable φ at a given position (x_k, y_l) of the 2D mesh, the resulting filtered field $\overline{\varphi}$ is

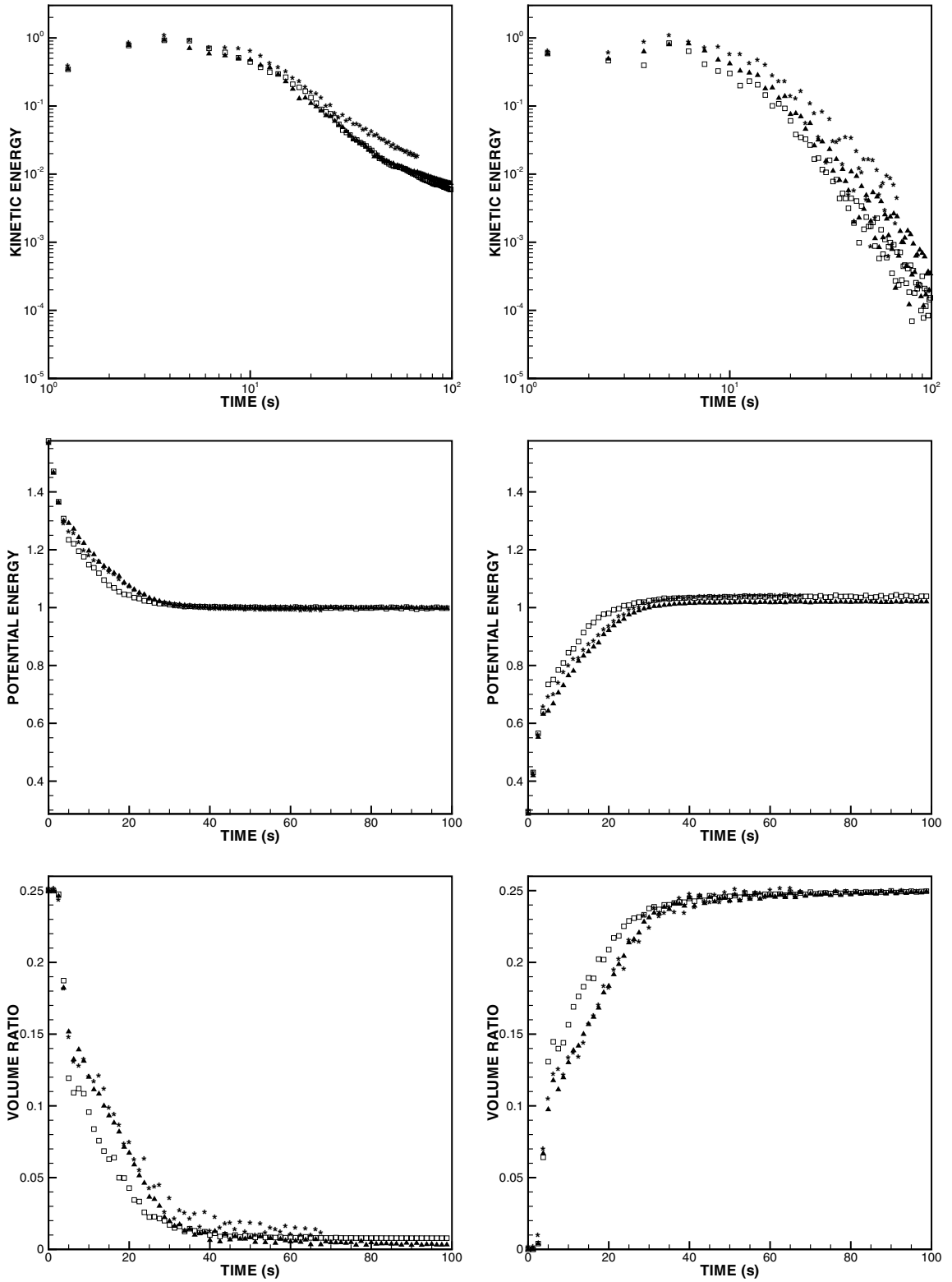

Fig. 9. Temporal evolution of macroscopic characteristics of the phase inversion problem – left column: water, right column: oil, from top to bottom: kinetic energy (log scale), potential energy and ratio between phase volume in the 1/4 upper cavity and total volume. □: 128×128 grid, ▲: 256×256 grid, ★: 512×512 grid.

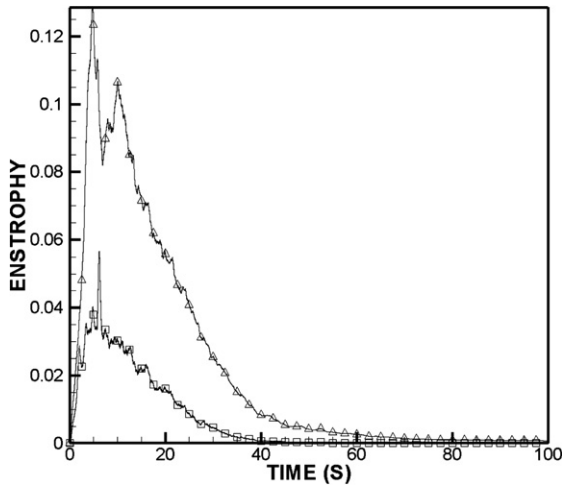

Fig. 10. Temporal evolution of enstrophy of the phase inversion problem – △: water, □: oil.

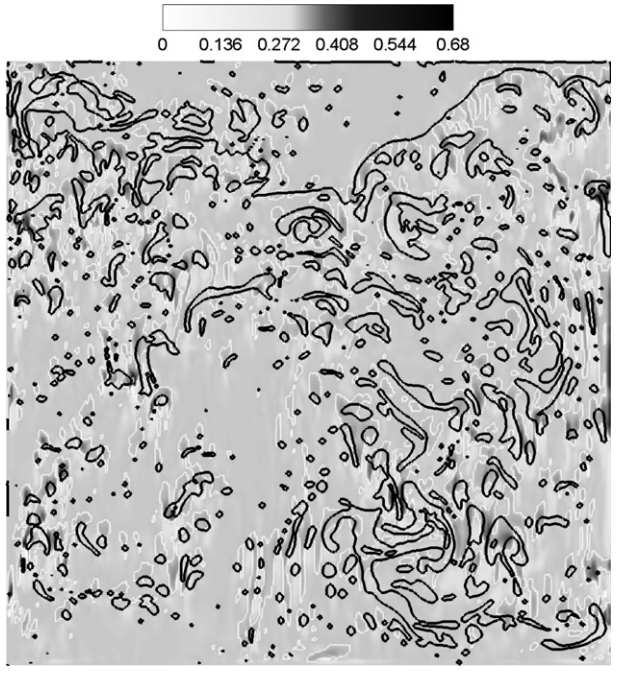

Fig. 11. Calculation of z-component of velocity tensor $\tau_{l\rho uu}$ with FiSm top-hat filtering.

$$\overline{\varphi} = \frac{1}{(2 * n_i + 1) * (2 * n_j + 1)} \sum_{i=-n_i, j=-n_j}^{n_i, n_j} \varphi(x_{k+i}, y_{l+j}) \tag{72}$$

where n_i and n_j account for the size of the filter, and verify the identity:

$$(2n_i + 1)\Delta x = \Delta X \tag{73}$$

$$(2n_j + 1)\Delta y = \Delta Y \tag{74}$$

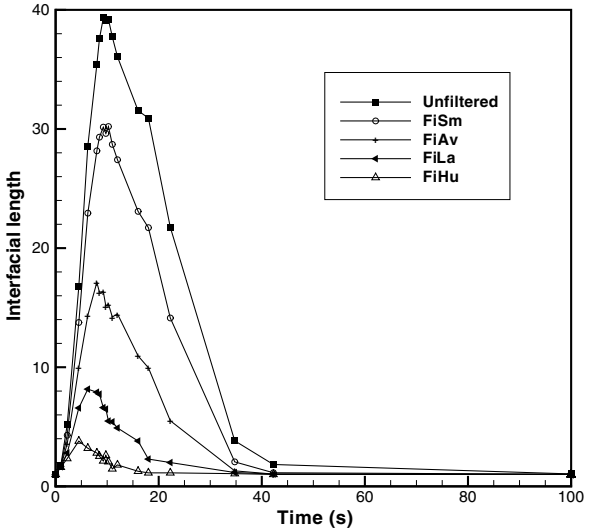

Fig. 12. Temporal evolution of interfacial lengths depending on the size of the filter.

6.1. Bubble test case

Four filter sizes (Huge, Large, Average, Small) are considered and applied to the previously described test cases. The first filter FiSm corresponds to a correctly resolved solution in terms of turbulence and interface LES. The second filter FiAv corresponds to a poorly resolved solution in terms of turbulence and correctly resolved in terms of interface LES. The third filter FiLa corresponds to a subgrid scale turbulence while under resolved interface LES. The last filter FiHu corresponds to subgrid scale bubble and turbulence. It is an interesting filtering size, since lot of recent papers use a filtering size at least two times bigger than the bubble size for the simulations (see, for instance, Lakehal et al., 2002).

The *a priori* test is at first carefully carried on the previously presented configurations. The sizes of the filters (equal to $\Delta X \Delta Y$, see Eq. (71)) employed are summarized in Table 3, in comparison with the surface corresponding to the mesh size of the DNS ($\Delta x \Delta y$), of the bubble (R_b) and of the "turbulent structures" (R_v). A similar table (Table 6) summarizes the corresponding filtering sizes for the phase inversion test case.

Before analyzing the magnitude of the different subgrid scale terms, we want to check that the commutation error is close to zero. Indeed, this error, only localized near the interface, remains clearly negligible in comparison with the maximum of the filtered convection $\nabla \cdot \overline{\rho u \otimes u}$. This small error is concentrated on the border of the filtering box. More generally, the calculation of the errors over the very fine DNS mesh, implies sometimes a false discontinuous feeling for the error field, which is only due to the high gradients involved.

The evolution of the maximal norm of the different subgrid-scale contributions with the time is plotted in Figs. 14 and 15 for the different sizes of the filter and for the test case (N0) of the slightly deformed bubble.

Before the impact, $\nabla \cdot \tau_{l\rho uu}$ is largely dominant compared to any other subgrid scale terms and whatever the filter size, which is a usual conclusion for single-phase turbulence. In this configuration, all the error terms except $\nabla \cdot \tau_{l\rho uu}$ can be ignored. In the case FiLa and FiHu, the maximum initial value of $\nabla \cdot \tau_{l\rho uu}$ is close to 1, meaning that the strong velocity gradients are very insufficiently resolved. That is not astonishing since the vortices are almost subgrid in these two cases. Figs. 14 and 15 give general information about the relative magnitude of the different terms. The temporal interval $[0.003, 0.004]$ corresponds to the time when vortices are generated in the gas phase and initial vortices are split apart and begin to roll along the interface of the bubble (see the third and fourth images of the set Fig. 2). This topological transformation leads to a jump of the term $\nabla \cdot \tau_{l\rho uu}$ in the case FiSm. In the much coarser FiLa case, these very large values of $\nabla \cdot \tau_{l\rho uu}$ persist during the calculation. The contribution of the diffusion is the second one, in terms of magnitude, in the well-resolved case FiSm. In the other cases, the term $\frac{\partial \tau_{l\rho u}}{\partial t}$ is of great importance, in that it is bigger than the diffusion. In the cases for which the interfaces are correctly resolved, that are FiSm and FiAv, the interfacial

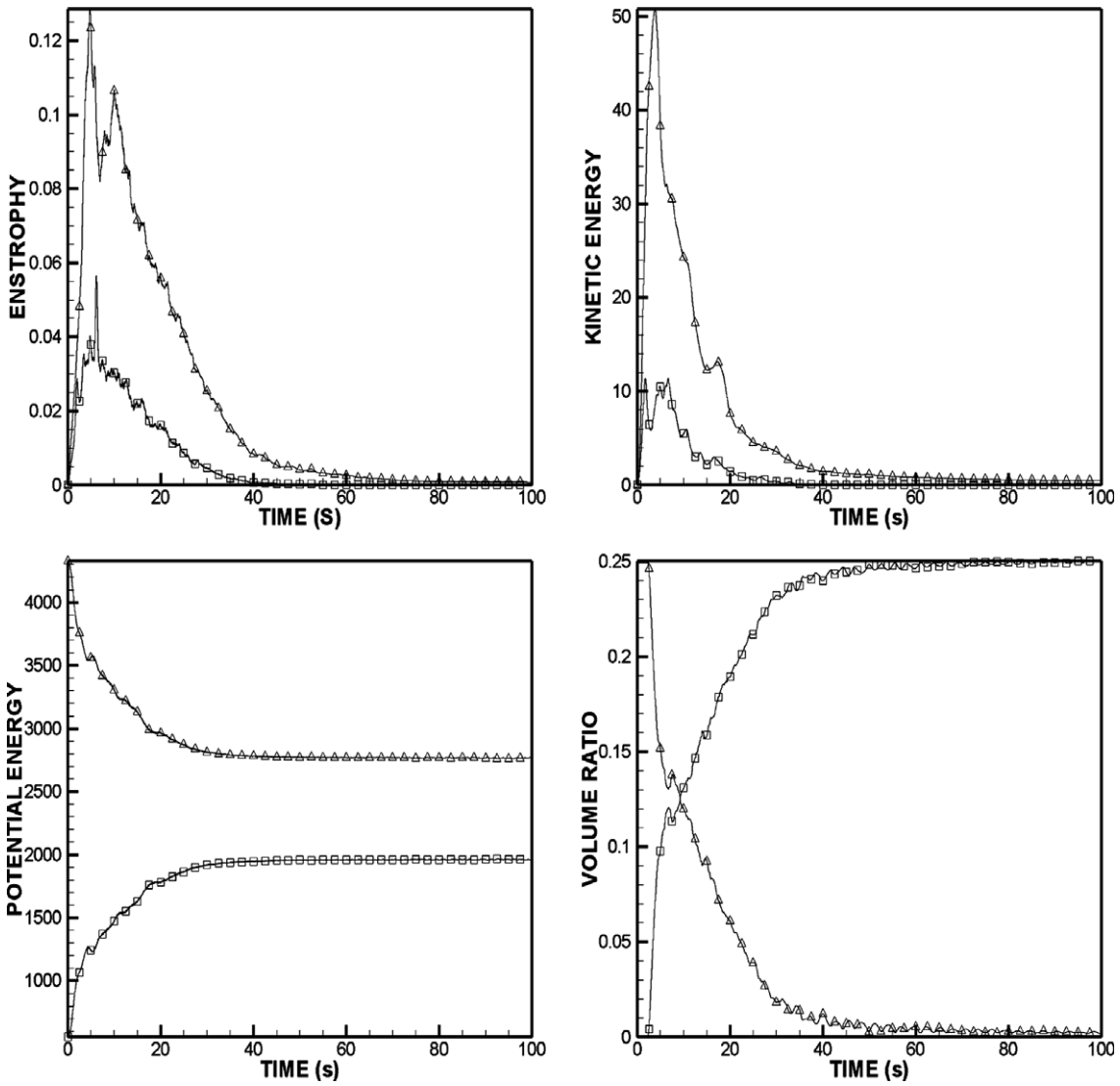

Fig. 13. Temporal evolution of macroscopic characteristics of the phase inversion problem from left to right and from top to bottom: enstrophy, kinetic energy, potential energy and ratio between phase volume in the 1/4 upper cavity and total volume. □: oil, △: viscous water.

Table 3
The four sizes of the filter

Filter	$\left(\frac{\Delta X \Delta Y}{\Delta x \Delta y}\right)^{1/2}$	$\left(\frac{\Delta X \Delta Y}{R_c^2}\right)^{1/2}$	$\left(\frac{\Delta X \Delta Y}{R_b^2}\right)^{1/2}$
FiSm (small)	5	0.19	0.1
FiAv (average)	21	0.75	0.4
FiLa (large)	41	1.5	0.8
FiHu (huge)	201	7.5	4

induced term τ_{rnn} is close to zero and clearly negligible. However, in the other cases FiLa and FiHu, it is of the same order as diffusion.

In the case FiHu, all the flow is entirely subgrid, and then $\nabla \cdot \tau_{l\rho uu}$ is always equal to the filtered convection term $\nabla \cdot \overline{\rho u \otimes u}$ (and then equal to 1 when normalized). The interest focuses on the relative magnitude of the

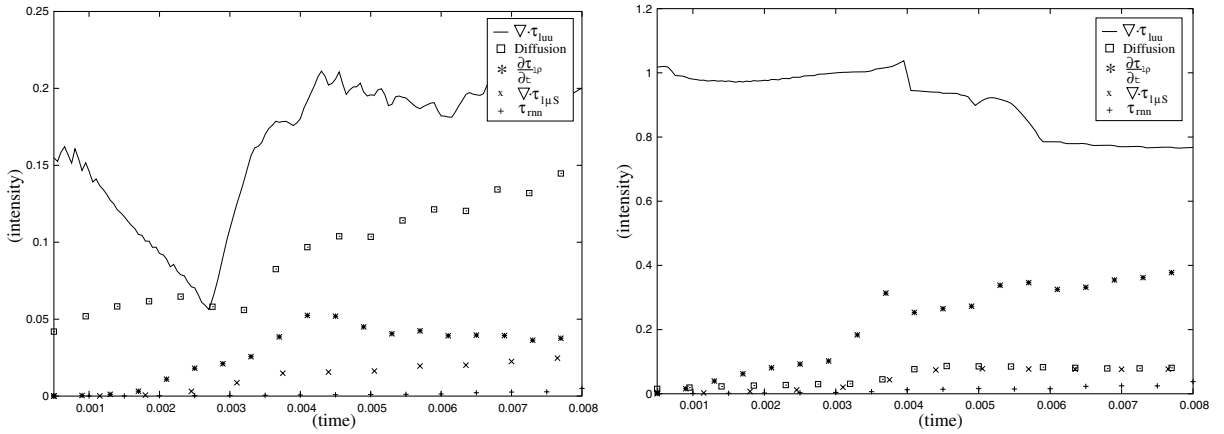

Fig. 14. Left: FiSm, right: FiAv. —: $\nabla \cdot \tau_{l\rho uu}$, □: diffusion, ∗: $\frac{\partial \tau_{l\rho u}}{\partial t}$, ×: $\nabla \cdot \tau_{l\mu S}$, +: τ_{rnn}.

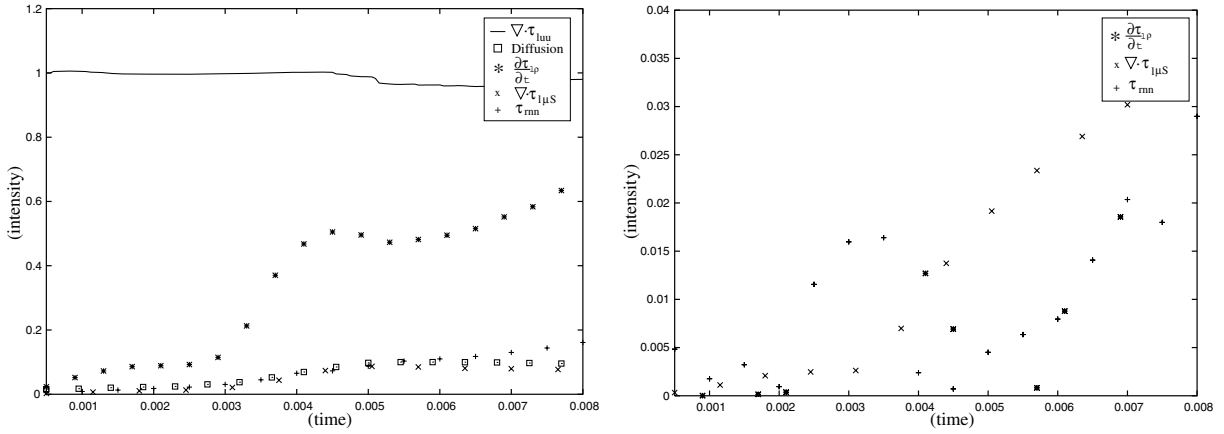

Fig. 15. Left: FiLa, right: FiHu. —: $\nabla \cdot \tau_{l\rho uu}$, □: diffusion, ∗: $\frac{\partial \tau_{l\rho u}}{\partial t}$, ×: $\nabla \cdot \tau_{l\mu S}$, +: τ_{rnn}.

other quantities. The magnitude of the diffusion $\nabla \cdot \tau_{l\mu S}$ increases but stays one order smaller in comparison to convection. The τ_{rnn} term is of the same order as the diffusion, but has an oscillatory behavior in agreement with the previous observations (see Section 5.2.2). Compared to FiLa, the magnitude of this term is quite low. This can be explained because the bubble is completely subgrid. Thus, considering the geometric nature of the term τ_{rnn}, we believe that the contributions of all the vectors τ_{rnn} over the spherical bubble compensate each other. The contribution of $\frac{\partial \tau_{l\rho u}}{\partial t}$ is of the same order of magnitude but slightly lower than the other ones. This surprisingly low value, in comparison with those obtained for FiLa for instance, lead us to conclude that symmetry effects reduce the order of magnitude of this term too.

The classical hierarchy of the subgrid scale terms seems to be respected for this case, and Table 4 summarizes these conclusions (the framed term vanish if the mass-weighted filtering process is used).

It is worth noting that when the turbulence (vortices) is mainly subgrid, we can write: $\nabla \cdot \overline{\rho u \otimes u} = \nabla \cdot \tau_{l\rho uu}$ and $\nabla \cdot \overline{\tau} = \nabla \cdot \tau_{l\mu S}$, in our case with no main stream.

To give more credit to these conclusions, a parametrical analysis has been undertaken thanks to the cases (N1) and (Solid).

It is worth noting that the bubble is much more distorted for the (N1) case than in the previous case. In the (Solid) case, the vortices rebound on the surface of the bubble. Strong strain is observed when the vortices encounter the bubble. The vortices are split apart and do not interact with each other anymore. Then, they disappear progressively thanks to the dissipation.

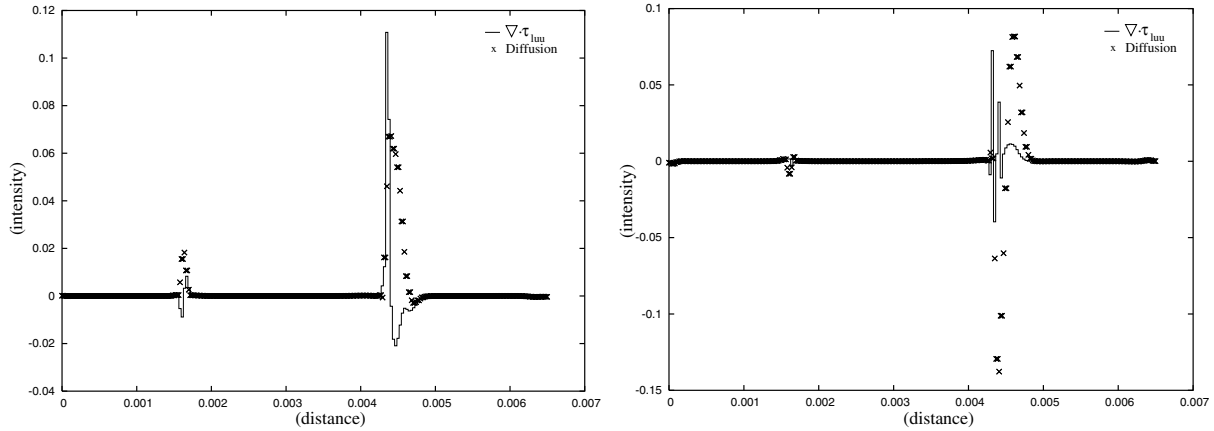

Fig. 16. Components of the acceleration: left: x component, right: y component – plain line: $\nabla \cdot \tau_{l\rho uu}$, symbols: diffusion.

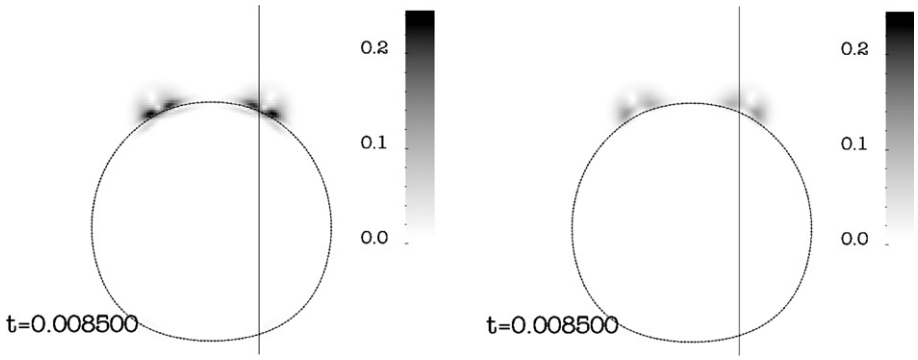

Fig. 17. Comparison of the isovalues of the terms $\nabla \cdot \tau_{l\rho uu}$ (left) and $\nabla \cdot \tau_{fl\rho uu}$ (right), FiSm filter.

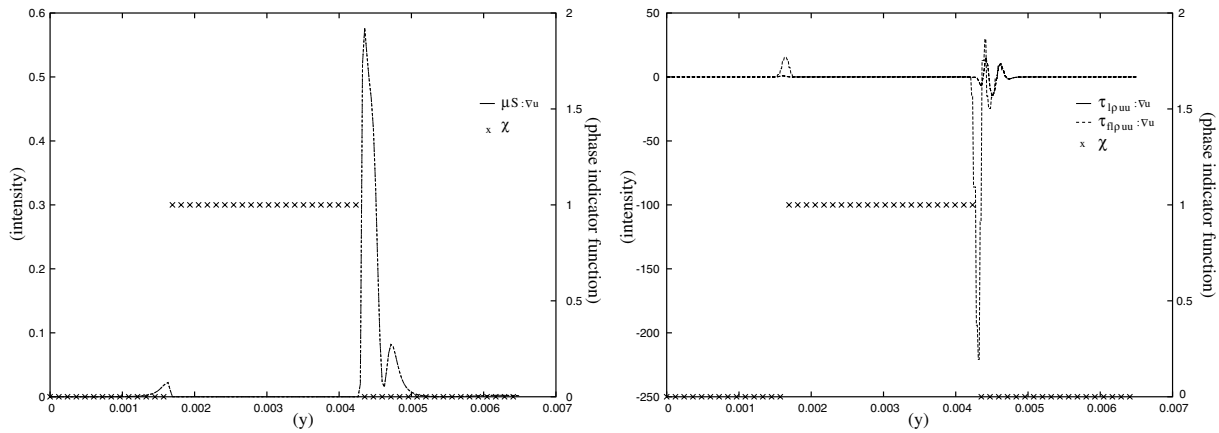

Fig. 18. Contribution to the kinetic energy balance. Left: plain line – $\mu S : \nabla u$, χ – phase indicator function. Right: plain line – $\tau_{l\rho uu}$: ∇u, dashed line – $\tau_{fl\rho uu}$: ∇u, χ – phase indicator function.

The evolution of the maximal norm of the different subgrid-scale contributions with the time is plotted in Figs. 21–23 for different sizes of the filter and for this new cases.

The first noticeable conclusion of this parametrical study lies in the astonishingly high value of the term $\frac{\partial \tau_{l\rho u}}{\partial t}$ for the case (N1). This is probably due to the low order of the time filtering derivative, which uses an Euler

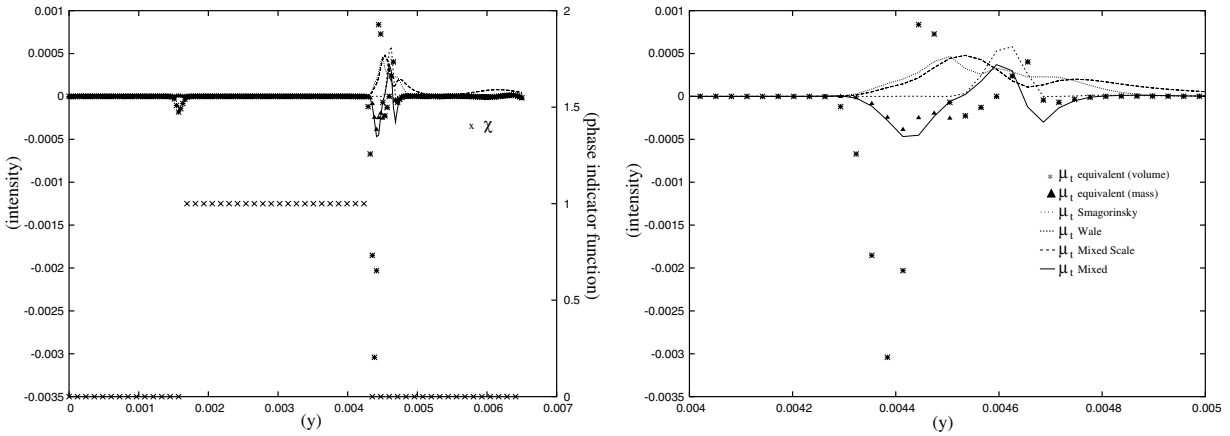

Fig. 19. Comparison between the μ_t *equivalent* obtained with the volume filter (*), μ_t *equivalent* obtained with the mass-weighted filter (▲), μ_t obtained using a Smagorinsky model (dotted line), μ_t obtained using a Wale model (short-dashed line), μ_t obtained using a Mixed Scale model (long-dashed line) and μ_t obtained using a Mixed Bardina–Smagorinsky model (plain line). χ – phase indicator function. Right: zoom at the vicinity of the interface.

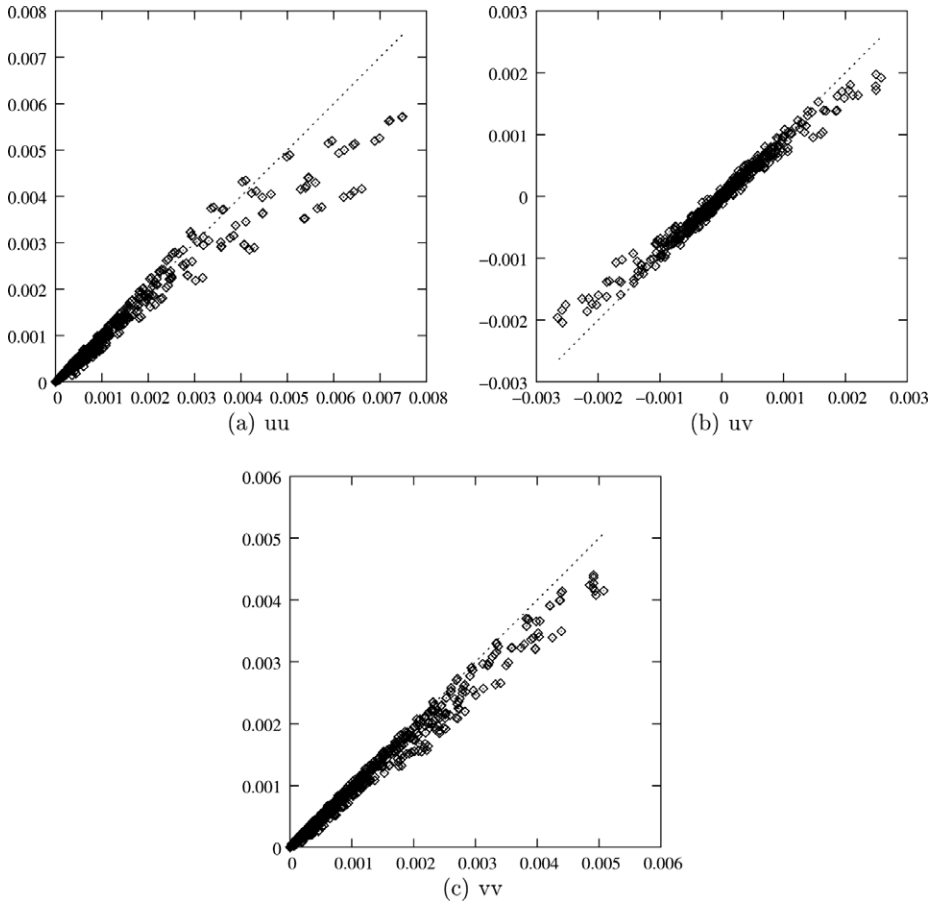

Fig. 20. Correlation: proposed mixed model (y axe) and real DNS contribution (x axe).

scheme. It seems that $\frac{\partial \tau_{lpu}}{\partial t}$ increases with the deformation rate of the shape of the bubble. Except for this term, most of the previous conclusions can be retrieved. The Kolmogorov scale being larger in these cases, and the

Table 4
Classification of the terms in the momentum equation for different filtering sizes

Category	FiSm	FiAv	FiLa	FiHu
Large	$\nabla \cdot \overline{\rho u \otimes u + p}$	$\nabla \cdot \overline{\rho u \otimes u + p}$ $\nabla \cdot \tau_{l\rho uu}$	$\nabla \cdot \overline{\rho u \otimes u + p}$ $\nabla \cdot \tau_{l\rho uu}$	$\nabla \cdot \overline{\rho u \otimes u + p}$ $\nabla \cdot \tau_{l\rho uu}$
Medium	$\nabla \cdot \tau_{l\rho uu}$ $\nabla \cdot \overline{\tau}$	$\boxed{\frac{\partial \tau_{l\rho u}}{\partial t}}$	$\boxed{\frac{\partial \tau_{l\rho u}}{\partial t}}$	
Small	$\boxed{\frac{\partial \tau_{l\rho u}}{\partial t}}$ $\nabla \cdot \tau_{l\mu S}$	$\nabla \cdot \overline{\tau}$ $\nabla \cdot \tau_{l\mu S}$	$\nabla \cdot \overline{\tau}$ $\nabla \cdot \tau_{l\mu S}$ τ_{rnn}	$\nabla \cdot \overline{\tau}$ $\nabla \cdot \tau_{l\mu S}$
Negligible	τ_{rnn}	τ_{rnn}		τ_{rnn} $\boxed{\frac{\partial \tau_{l\rho u}}{\partial t}}$

Table 5
Parametrical differences with the reference case

	$\omega_{\max}(t=0)$	$R_v(t=0)$	$V_M(t=0)$	$\eta(t=0)$	V_{vortex}
N0	30,000	4×10^{-4}	12.52	10^{-5}	2.54
N1	600	8×10^{-4}	0.77	6×10^{-5}	0.2
Solid	30,000	4×10^{-4}	12.52	10^{-5}	2.54

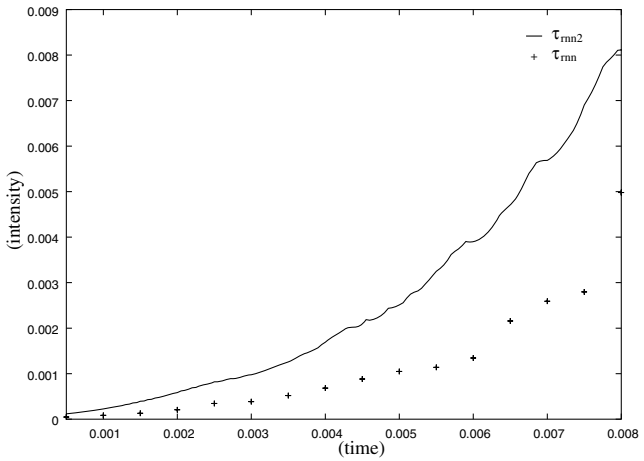

Fig. 21. Comparison between the maximal norm of τ_{rnn2} (plain line) and τ_{rnn} (symbols).

mesh used being the same as in the previous calculation, the vortices are never completely subgrid, but in the case of the filter FiHu. For the two cases, the jump of $\nabla \cdot \tau_{l\rho uu}$ is present, corresponding to the impact of the vortices with the bubble. The oscillatory behavior of the $\nabla \cdot \tau_{l\rho uu}$ term, which is particularly noticeable on the right of Fig. 22 corresponds to the vortices frequency. This frequency decreases abruptly when the vortices impact the bubble, which corresponds to a more coherent turbulence.

In the (Solid) case, it can be observed that the mechanical energy decreases more quickly than in the bubble case. This means that part of the energy is stored in the deformable bubble interface and not in the solid one. Moreover, all the subgrid terms except $\nabla \cdot \tau_{l\rho uu}$ are negligible. The comparison of the evolution of this term for the first case and the (Solid) case is presented in Fig. 24. It is observed that the behavior of $\nabla \cdot \tau_{l\rho uu}$ differs clearly. Until impact with the bubble, the behavior of the two curves is very similar. When impacting the bubble, the production of subgrid scale term $\nabla \cdot \tau_{l\rho uu}$ is even stronger in the bubble case. However, after the impact, the continuity of the velocity through the interface seems to contribute to maintaining a high level of $\nabla \cdot \tau_{l\rho uu}$ in the first case, while it decreases quickly in the (Solid) case. On the other hand, the order of mag-

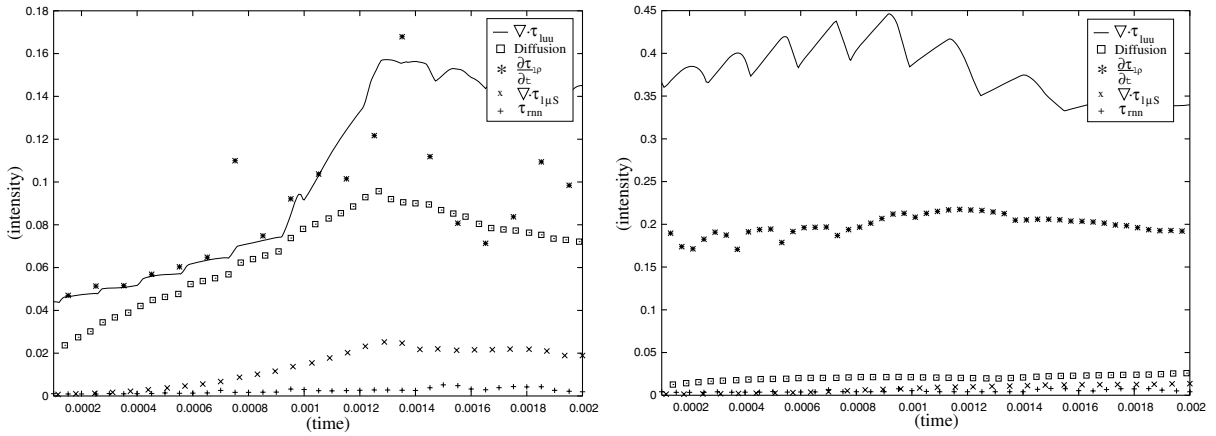

Fig. 22. N1 – left: FiSm, right: FiAv. —: $\nabla \cdot \tau_{l\rho uu}$, □: diffusion, ∗: $\frac{\partial \tau_{l\rho u}}{\partial t}$, ×: $\nabla \cdot \tau_{l\mu S}$, +: τ_{rnn}.

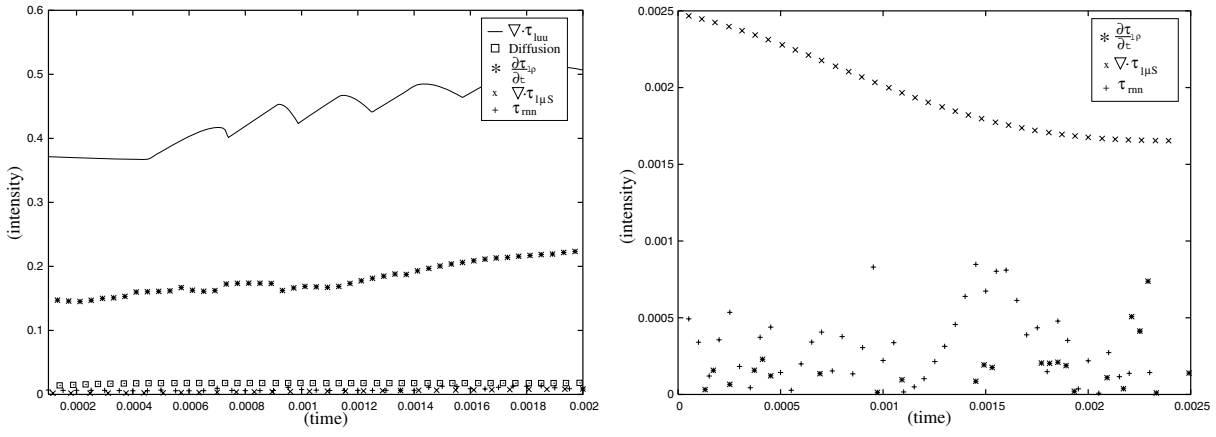

Fig. 23. N1-Left: FiLa, Right: FiHu. —: $\nabla \cdot \tau_{l\rho uu}$, □: diffusion, ∗: $\frac{\partial \tau_{l\rho u}}{\partial t}$, ×: $\nabla \cdot \tau_{l\mu S}$, +: τ_{rnn}.

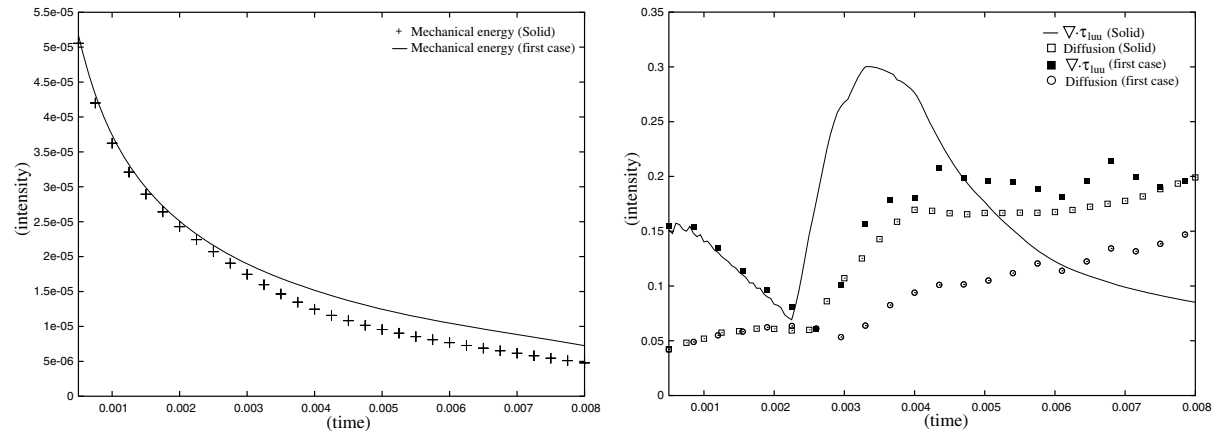

Fig. 24. Comparison between the first case and the (Solid) case – left: mechanical energy – plain line: first case, symbols: (Solid) case. Right: subgrid and diffusion terms maximal norm. —: $\nabla \cdot \tau_{l\rho uu}$ (Solid), ■: $\nabla \cdot \tau_{l\rho uu}$ (first case), □: diffusion (Solid), ○: diffusion (first case).

Table 6
The four sizes of the filter

Filter	$\left(\frac{\Delta X \Delta Y}{\Delta x \Delta y}\right)^{1/2}$
FiSm (small)	2
FiAv (average)	4
FiBi (big)	8
FiLa (large)	16

nitude of diffusion is greatly increased by the impact and becomes quickly bigger than the $\nabla \cdot \tau_{l\rho uu}$ in the (Solid) case. We then retrieve, as for the energy comparison, that the deformation of the interface stores the energy, which is then dissipated much slower.

6.2. Phase inversion test case

In this section, the same top-hat filter is implemented as detailed in Eq. 71 and a "phase-weighted" filtering is applied to the fields (Eq. 37). The sizes of the filtering kernels are detailed in Table 6. Moreover, all the tensor magnitudes are normalized by the time maximum for the 2D-plots (Figs. 11 and 25–28) and by the maximum tensor magnitude at each considered time for the spatial averaged tensor values (Tables 7–9).

As previously, four different sizes of the filter are proposed, from a 2×2 stencil up to a 16×16 stencil. One example of subgrid error tensor corresponding to the smallest filter size is presented in Fig. 11. As expected, the larger the filter is, the greater the magnitude of the subgrid tensors is. A close inspection of the local variations of the different tensor magnitudes reveals the highest values are located near the interfaces whereas a homogeneous, but non-zero, behavior is observed within the two phases. It is also observed that even in highly turbulent areas located in oil or viscous water and when turbulence reaches its maximum, the magnitudes of the subgrid tensors are smaller than the values at the interface.

Tables 7 and 8 summarize the differences corresponding to these 2D views. Clearly, the mixing process leads to higher gradient in the z-direction (gravity) than in the x-direction, and thus to higher values of the subgrid accelerations in this direction. In this case, capillarity and diffusivity are the driving mechanisms, and the corresponding subgrid terms τ_{rnn} are almost of the same order of magnitude as $\tau_{l\rho uu}$ for the smaller filter sizes. Fortunately, the classical $\tau_{l\rho uu}$ subgrid terms remain dominant, at least when the field is highly unsteady. Indeed, the values of τ_{rnn} are surprisingly high at the end of the calculation, when only small droplets of oil subsist. It can be deduced that the capillary term is proportional to the curvature, which is higher when the inclusions are small, whereas the convection term is proportional to the velocity, which is small for small droplets.

The evolution of the order of magnitude of the different subgrid terms with the filter size is presented in Table 8 for the time $t = 2.25$ s. As expected, the magnitude of the $\tau_{l\rho uu}$ term increases with the filter size. On the contrary, the magnitude of τ_{rnn} decreases with the filter size. The explanation is that many inclusions are completely subgrid when the filter size is large. Thus, as already stressed before, symmetry consideration on the subgrid error makes the integral contribution lower than if a smaller filter size[5] is considered.

Table 9 sorts the mean tensor magnitudes into 4 categories equally balanced between 0.01 and 1. As previously observed and as expected, the inertial tensor becomes predominant as soon as the filter size grows. On the contrary, the surface tension tensor is large for the smaller filter while it decreases to a weaker influence. As a matter of fact, at instant $t = 9.75$ s, numerous small droplets are advected in the flow, and thus tend to vanish as they become subgrid. The behavior described previously remains true as long as the flow is turbulent ($t \leqslant 30$ s in this case), while, as shown for example in Table 8, only the surface tension tensor is significant as the turbulence vanishes.

To finish with, the interfacial area is a major parameter controlling mass and energy transfers in two-phase flows. It is a quantity used in to close most of the statistical two-phase turbulence models (see for instance the works of Prince and Blanch (1990), Yao and Morel (2004)) and has to be considered in this work. Whereas the subgrid rate of interfacial area is nearly zero (less than 0.1%) in the previous test case with weakly disturbed

[5] With no subgrid inclusion.

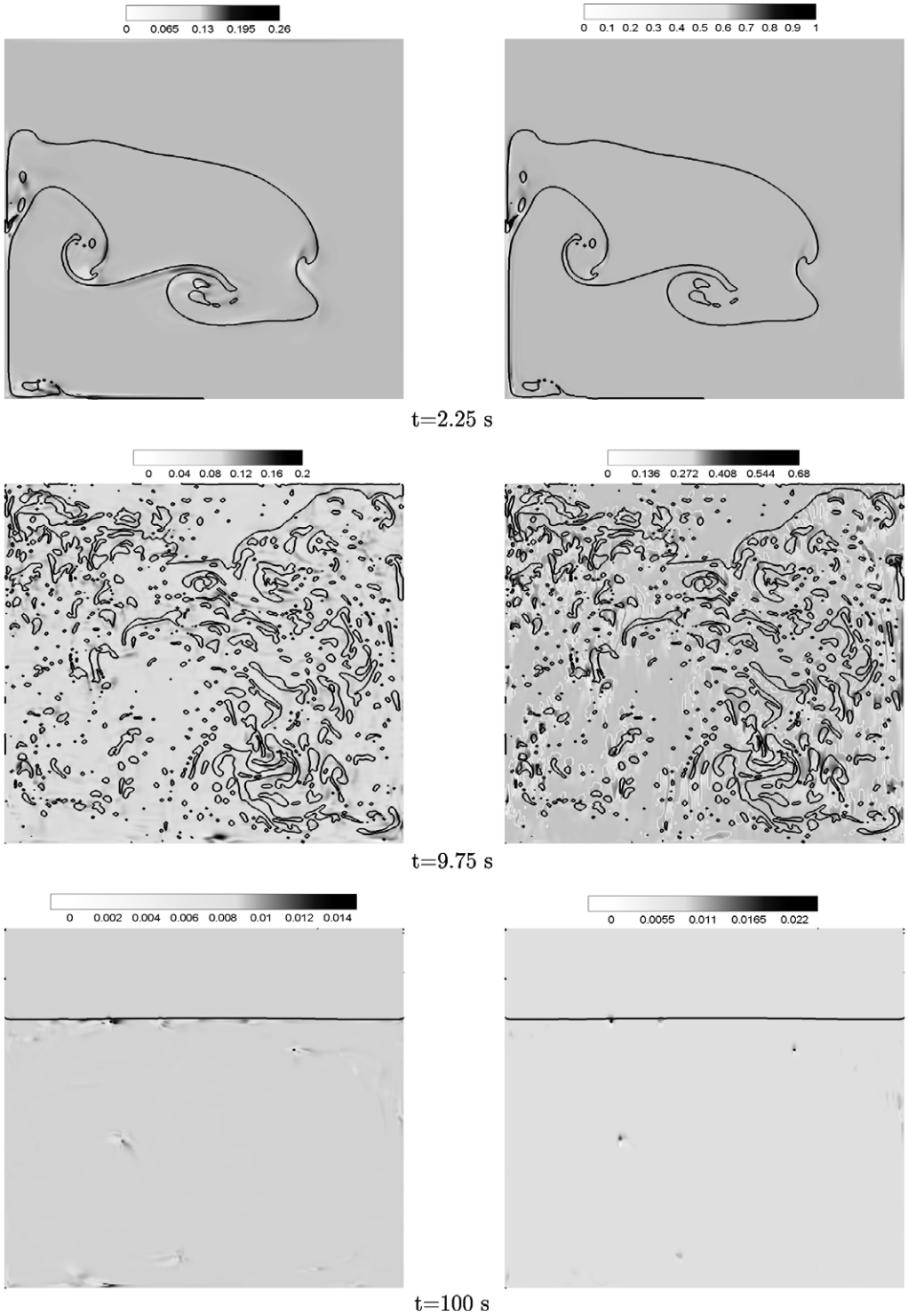

Fig. 25. Calculation of velocity tensor $\tau_{l\rho uu}$ with FiSm top-hat filtering (left column: x-component, right column: z-component).

interface, it is not the case in this capillarity driven test case. Its temporal evolution has thus been considered here. As soon as filter based turbulence models will be implemented to simulate two-phase flows, the effect of

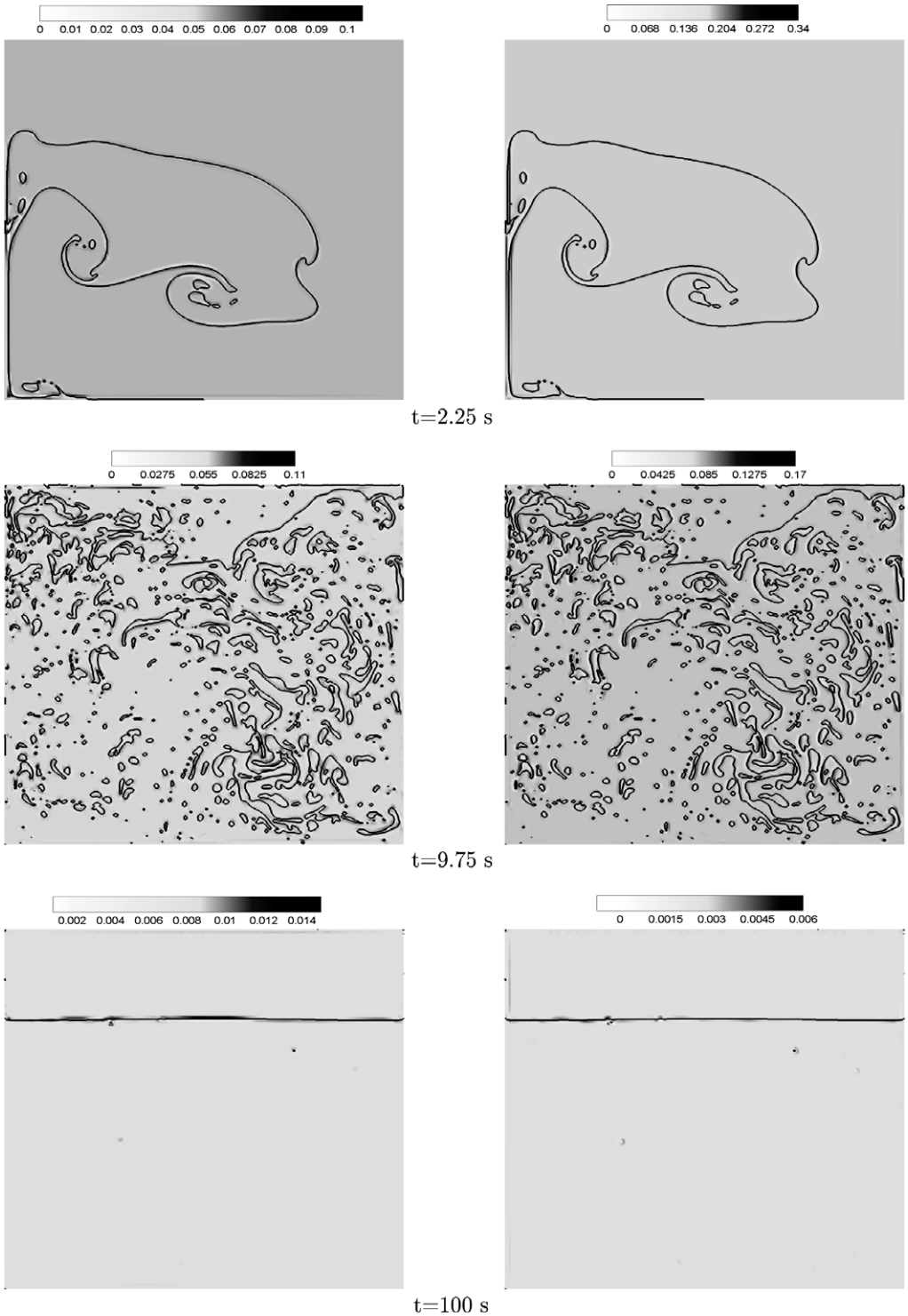

Fig. 26. Calculation of viscosity tensor $\tau_{l\mu S}$ with FiSm top-hat filtering (left column: x-component, right column: z-component).

the filtered scale on the interfacial area is investigated in Fig. 12. As expected, the larger the size of the filter is, the smaller the interfacial area is. Quantitatively, a FiSm filtering induces a 25% loss of maximum interfacial

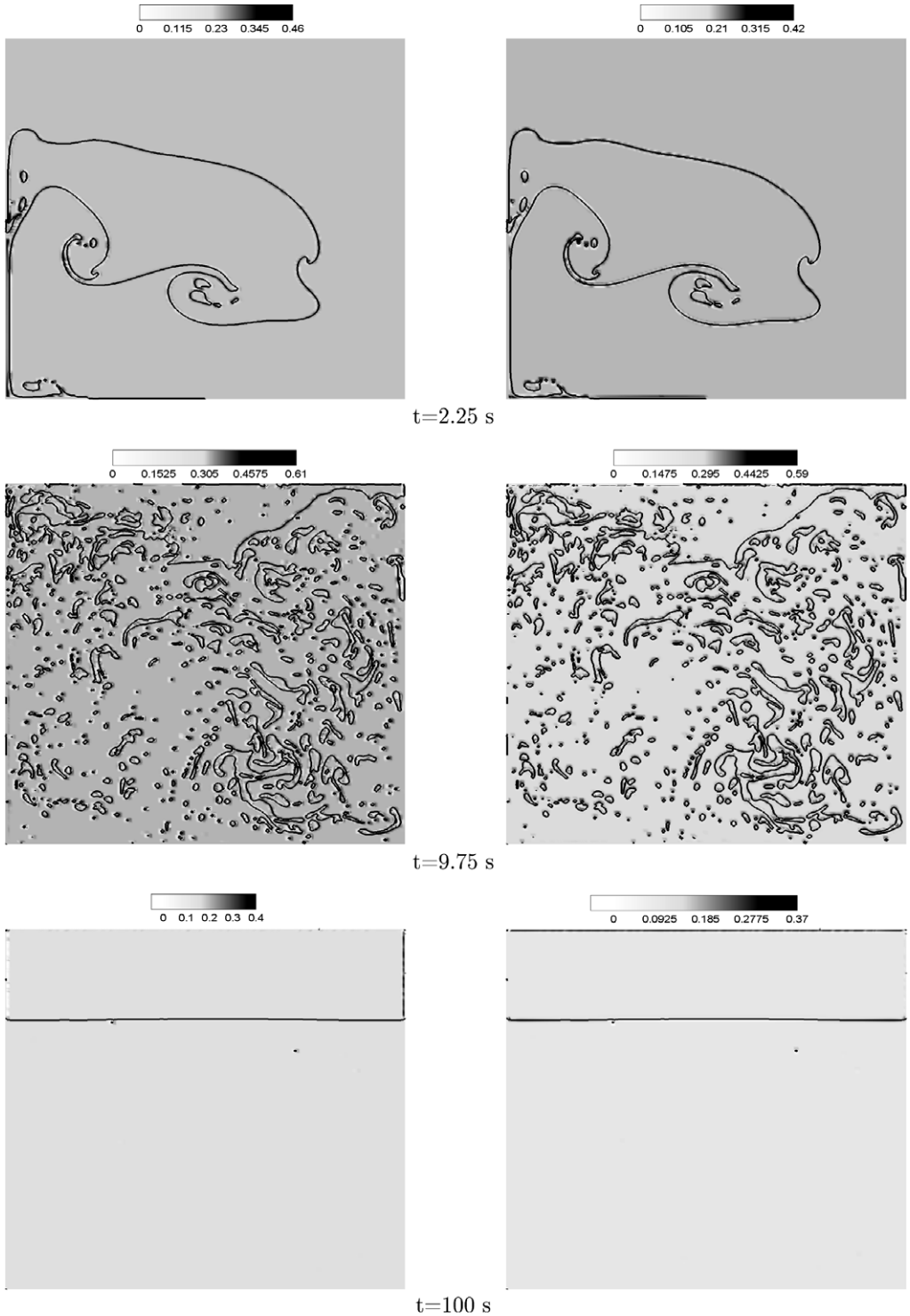

Fig. 27. Calculation of surface tension tensor τ_{rnn} with FiSm top-hat filtering (left column: x-component, right column: z-component).

length of the DNS one whereas a FiHu filtering decreases the magnitude to 90%. When standard single-phase LES turbulence models will be used, the huge effect of the filtering on the interfacial area will be responsible of

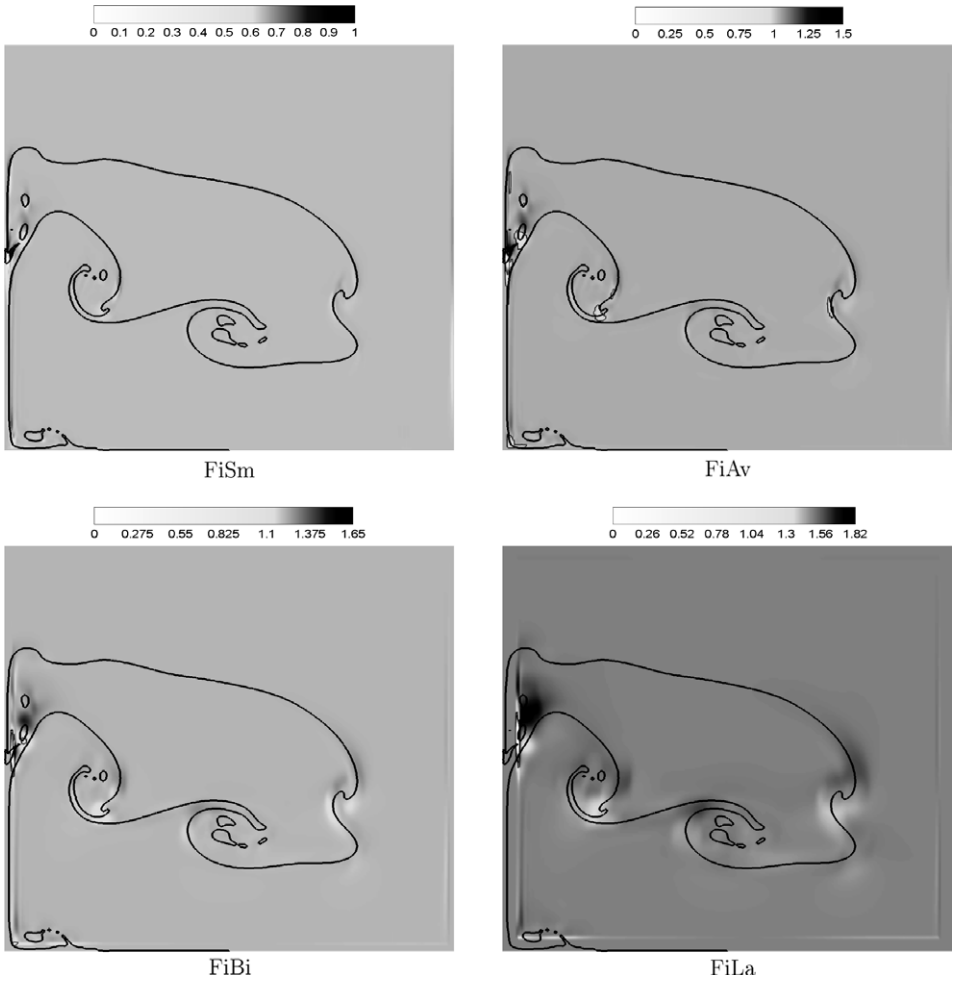

Fig. 28. Spatial filtering of the z-component of velocity tensor $\tau_{l\rho uu}$. The results are presented at instant 2.25 s.

Table 7
Range evolution of tensor magnitude for instants $t = 2.25, 9.75, 100$ s

Filter size	Time (s)					
	2.25		9.75		100	
	FiAv	FiBi	FiAv	FiBi	FiAv	FiBi
$\tau_{l\rho uu}$ (x-component)	0.368	0.785	0.254	0.660	0.018	0.030
$\tau_{l\rho uu}$ (z-component)	0.567	1	0.453	1	0.020	0.032
$\tau_{l\mu S}$ (x-component)	0.087	0.103	0.066	0.087	0.015	0.016
$\tau_{l\mu S}$ (z-component)	0.231	0.222	0.148	0.180	0.020	0.022
τ_{rnn} (x-component)	0.618	0.510	0.558	0.542	0.247	0.238
τ_{rnn} (z-component)	1	0.813	1	0.957	1	1

dramatic differences between DNS and LES simulations of two-phase flows. A specific attention will have to be paid to integrating a resolved subgrid volume fraction in interface tracking methods in order to add explicit modeling of interfacial subgrid tensors taking into account the filtered interfacial areas.

Table 8
Evolution of tensor magnitudes at time 2.25 s for several spatial filtering sizes

Spatial filtering	FiSm	FiAv	FiBi	FiLa
$\tau_{l\rho uu}$ (x-component)	0.0931	0.368	0.785	0.819
$\tau_{l\rho uu}$ (z-component)	0.285	0.567	1	1
$\tau_{l\mu S}$ (x-component)	0.055	0.0867	0.103	0.052
$\tau_{l\mu S}$ (z-component)	0.202	0.231	0.222	0.110
τ_{rnn} (x-component)	0.625	0.618	0.510	0.225
τ_{rnn} (z-component)	1	1	0.813	0.355

Table 9
Classification of the terms in the momentum equation for different filtering sizes at time $t = 9.75$ s

Category	FiSm	FiAv	FiBi	FiLa
Large	$\tau_{rnn,x}$ $\tau_{rnn,z}$	$\tau_{rnn,x}$ $\tau_{rnn,z}$	$\tau_{rnn,x}$ $\tau_{rnn,z}$ $\tau_{l\rho uu,x}$ $\tau_{l\rho uu,z}$	$\tau_{l\rho uu,x}$ $\tau_{l\rho uu,z}$
Medium	$\tau_{l\rho uu,x}$ $\tau_{l\rho uu,z}$	$\tau_{l\rho uu,x}$ $\tau_{l\rho uu,z}$ $\tau_{l\mu S,z}$	$\tau_{l\mu S,z}$	$\tau_{rnn,x}$ $\tau_{rnn,z}$ $\tau_{l\mu S,z}$
Small	$\tau_{l\mu S,z}$	$\tau_{l\mu S,x}$	$\tau_{l\mu S,x}$	$\tau_{l\mu S,x}$
Negligible	$\tau_{l\mu S,x}$			

6.3. Modeling attempts

To conclude this study, some modeling attempts have been made to handle the particular behavior of the turbulence at the vicinity of the interfaces. It can be seen that in using $\bar{u}$ (volume filtering process), the momentum transfer is widely overestimated, whereas it is underestimated in using $\tilde{u}$ (mass-weighted filtering process). It is illustrated with Fig. 17. Thus, it is demonstrated that the use of $\tilde{u}$ is recommended for two-phase flow turbulence modeling. At first, the error term $\tau_{l\rho u}$ becomes zero in using $\tilde{u}$. Moreover, the method is less diffusing than in using $\bar{u}$, what is easier to model.

It seems necessary, since the behavior of the main subgrid contribution $\nabla \cdot \tau_{l\rho uu}$ is clearly unusual. Fig. 16 shows the x and y components of $\nabla \cdot \tau_{l\rho uu}$ and of the diffusion term, for the FiSm filter and for the (N0) case.

These graphics are extrapolated from the values on the black line materialized in Fig. 17. It is worth noting that the peak of the diffusion term is mainly in the liquid phase, whereas, surprisingly, the $\nabla \cdot \tau_{l\rho uu}$ contribution reaches a maximum in the gas phase. This means that the subgrid dynamics cannot correctly be mimicked by the stress tensor only. Moreover, the temporal evolution of the subgrid terms is not correctly reproduced by that of the diffusion term, in particular for the jump of $\nabla \cdot \tau_{l\rho uu}$ when vortices are impacting the bubble (see the left part of Fig. 14). In fact, it appears clearly that the high level of error in the gas phase corresponds to a too high diffusion of the kinetic energy through the interface, thanks to the convection term.

Due to the one-fluid formulation, the momentum of the gas phase is spuriously transmitted to the liquid phase, because of the continuity of the velocity. That means that kinetic energy is immediately transmitted to the liquid phase of the calculation cells. It is worth noting that this feature is not sensitive for the steady states or for the very fine meshes, since the real characteristic time of kinetic energy transfer scales in l^2/ν. At the contrary, it is a very important feature in the case of highly unsteady flows and coarse meshes. The use of the mass-weighted average allows to drastically lowering this over-diffusivity, even implying an under-estimated diffusion rate. It can be easily corrected in adding a turbulent viscosity to the molecular viscosity in the momentum equation.

These conclusions can be completed with an energetic analysis. In order to perform this analysis, let decompose the action of $\tau_{l\rho uu}$ into a conservative part and a non-conservative part in order to obtain the resolved kinetic energy balance[6]:

[6] For the sake of simplicity, all subgrid terms but $\tau_{l\rho uu}$ have been neglected in this equation, and the overlines, tildes and hats are omitted.

$$\frac{\partial e_c}{\partial t} + \nabla \cdot ((e_c u)) + u \cdot \nabla p - \nabla \cdot (\tau \cdot u) + \tau : \nabla u - \nabla \cdot (\tau_{l\rho uu} \cdot u) + \tau_{l\rho uu} : \nabla u = -\sigma n \cdot W \nabla_s \cdot n \delta_i \tag{75}$$

The idea of the Boussinesq analogy for the turbulence is to consider that the main effect of the subgrid scale turbulence is of dissipative nature. The only subgrid term able to modify the global kinetic energy is $\tau_{l\rho uu} : \nabla u$ which is the counterpart for the subgrid tensor of the dissipation $\mu S : \nabla u$. These two terms ($\tau_{l\rho uu} : \nabla u$ and $\mu S : \nabla u$) are plotted in Fig. 18.

The left-hand-side of Fig. 18 shows the spatial profile of the dissipation. The highest peak is located in the vicinity of the interface at the top of the bubble. A second one is close to the center of the vortex in the liquid phase (see Fig. 17), and a third (smaller) one is located close to the interface at the bottom of the bubble. The right-hand-side of Fig. 18 shows the counterpart of the dissipation for the subgrid stress tensors obtained using the volume filtering process ($\tau_{l\rho uu}$) and the mass-weighted filtering process ($\tau_{fl\rho uu}$). The first remark is that the magnitude of these terms is one to two orders bigger than those of the dissipation, that is a classical feature of turbulent flows. The behavior of these two terms seems similar, with a first positive peak near the interface at the bottom of the bubble, and a negative peak near the interface at the top of the bubble. There is then a positive peak in the liquid phase. The negative peak in the vicinity of the interface is much bigger in the volume filtering case. It corresponds to an over-diffusivity of the kinetic energy of the liquid phase into the gas phase, what is strengthened by the peak in the liquid phase. This behavior is similar to what is observed for particle-laden flow (see Boivin et al., 2000).

Finally, the *equivalent eddy-viscosity* has been computed for this two filtering process, and compared with several classical closure models. The *equivalent eddy-viscosity* is calculated the following way:

$$\mu_t = \frac{\tau_{l\rho uu} : \nabla u}{S : \nabla u} \tag{76}$$

considering that an eddy-viscosity assumption implies that $\tau_{l\rho uu} = \mu_{tS} : \nabla u$. These results are plotted in Fig. 19.

Large eddy simulation is not suited for 2D flows because there is generally no energy cascade. However, the viscosity models do not naturally cancel in the limit of two-dimensional flows, and then comparison with the subgrid scale models give interesting pieces of information on the modeling process even in this case.

Obviously, the behavior of the *equivalent* μ_t matches those of the contribution of the subgrid tensors to the total kinetic energy balance (see Fig. 18), and the so-called *viscosities* obtained this way are locally negative close to the interface at the top of the bubble.

The negative part of the *equivalent* μ_t is by far bigger when the volume filtering process is employed. Nevertheless, for the positive part of *equivalent* μ_t, the two curves merge. The negative part of this *a priori closure* demonstrates that eddy-viscosity models are inadequate to model the subgrid scales in two-phase flows and that a dispersive phenomenon is of great importance. This is confirmed by the profiles of classical closure models based on an eddy-viscosity assumption. The Smagorinsky (Smagorinsky, 1963), the Wale (Nicoud and Ducros, 1999) and the Mixed-Scale models (Sagaut et al., 1999) are plotted in Fig. 19 and show similar behaviors and orders of magnitude, but obviously fail in mimicking the negative part of the *equivalent* μ_t. Nevertheless, Boivin et al. (2000) succeed in obtaining the right behavior of the *eddy-viscosity* in using mixed Bardina-like–Smagorinsky-like models (Bardina et al., 1983) *a.k.a.* the sum of a scale-similarity model and an eddy-viscosity assumption model. This model is also plotted in Fig. 19, and shows great improvements in modeling the *equivalent* μ_t (mass-weighted), in particular in the negative part, whereas the positive peaks do not match perfectly. This model seems to be a good preliminary choice to perform LES on two-phase flow configuration.

Fig. 20 shows the correlation between the previously proposed Bardina-like–Smagorinsky-like mixed model and the real DNS contribution on every cell of the FiSm coarse grid for the cases (N1). The error committed in using this model is less than 20% everywhere. That is close to the results obtained for single-phase flows by Horiuti (1997) (Figs. 11 and 25–28).

7. Conclusions

This original study is a preliminary step towards complete modeling of the interaction between interface and turbulence. The governing equations for under-resolved systems have been fully written and discussed for both RANS and LES approaches. In particular, specific multiphase terms have been exhibited.

Academic test cases mimicking the turbulence–interface interaction have been simulated. A special Front-Tracking method has been used for modeling the test case of vortices impacting on a bubble. A VOF approach has been adopted for the test case of the phase inversion in a closed square box. A phenomenological analysis of the evolution of the kinetic energy shows the importance of the interfacial terms in the turbulent behavior. The interface absorbs a part of the turbulent high-frequency energy and releases it at a lower frequency due to the interface oscillations. It is also shown that the interface can be considered in a sense as a deformable wall, at least if only one of the two phases is considered. Nevertheless, turbulence can be carried from one phase to another through the interface.

A priori tests have been conducted to provide information on the order of magnitude of the subgrid terms that arise with under-resolved calculation (RANS, LES). The relative importance of these terms has been carefully compared. The strategy consists in filtering the results of a DNS in order to provide the error terms that have to be modeled in RANS or LES approaches. Four different sizes of filter have been used on undisturbed, weakly disturbed and strongly deformed interfaces. The main conclusion is that the most important term remains the inertia term as in single-phase flows. However its behavior is clearly different close to the interface and can no longer be modeled with a viscosity assumption. This important conclusion has to be moderated if the mass-weighted filtering process is employed. This process is highly recommended for the modeling of turbulence in two-phase flows, when it is possible. The other terms are weaker, but not negligible compared to the diffusion term. It is also stated that the behavior of turbulent structures and subgrid scale terms is very different when solid surfaces are considered. At impact, the production of turbulence is stronger with solid bodies, but is not maintained at a high level for a long time as with bubbles. Moreover, the jump of the diffusion in the solid case when impacting the bubble is higher. It can be deduced that the bubble stores a part of the vortices' energy.

When considering flows driven by capillarity and viscosity mechanisms, the conclusions have to be moderated. The classical subgrid acceleration remains the dominant term, but the terms corresponding to the viscosity jump, and the capillary forces are almost of the same order. That is not astonishing, since these flows are mainly driven by capillarity effects, and are turbulent in another sense peculiar to two-phase flows (*interfacial turbulence*). This implies very challenging new modeling processes beyond the scope of this paper. Nevertheless a preliminary step for the modeling of the capillarity-induced term τ_{rnn} is proposed.

The inertia subgrid term is compared, in term of diffusivity, with several classical subgrid models. A model is provided which reproduce the correct behavior of the inertia subgrid term. A mixed Bardina-Smagorinsky model gives very satisfactory results, far better than the eddy-viscosity based models, which fail to reproduce the turbulence rate exchange.

Further works will focus on *a priori* tests on homogeneous isotropic turbulence and of classical single-phase subgrid modeling in three-dimensional two-phase flows, in order to study the effect of the Taylor microscale turbulence on interfaces. If none of the classical models give satisfactory results (what is expected in the case of highly deformable interfaces), the development of two-phase specific flow models will become necessary. We expect that a good modeling process will allow us to simulate more complex physics without using a *true* DNS approach. Future research will focus on the production of *quasi-turbulence* by the bubble wakes, turbulent dissipation in rollers when waves break on beaches (see Peregrine, 1983; Lubin et al., 2003), impinging turbulent plane jets on liquid films (see Lacanette et al., 2002) and boiling flows (see Juric and Tryggvason, 1998).

References

Bardina, J., Ferziger, J.H., Reynolds, W.C., 1983. Improved turbulence models for large eddy simulation. In: AIAA Paper 83-1357.

Batchelor, G.K., 1974. Transport properties of two-phase materials with random structure. Annu. Rev. Fluid Mech. 6, 227–255.

Boivin, M., Simonin, O., Squires, K.D., 2000. On the prediction of gas–solid flows with two-way coupling using large eddy simulation. Phys. Fluids 12, 2080–2090.

Brackbill, U., Kothe, D., Zemach, C., 1992. A continuum method for modelling surface tension. J. Comput. Phys. 100, 335–354.

Calmet, I., Magnaudet, J., 2003. Statistical structure of high-Reynolds-number turbulence close to the free surface of an open-channel flow. J. FLuid Mech. 474, 355–378.

Calvin, C., Cueto, O., Emonot, P., 2002. An object-oriented approach to the design of fluid mechanics software. Math. Modell. Numer. Anal. 36, 907–921.

Chandrasekhar, S., 1981. Hydrodynamic and Hydromagnetic Stability. Dover Publications, New York.

Christensen, E., Deigaard, R., 2001. Large eddy simulation of breaking waves. Coastal Eng. 42, 53–86.
Dakhoul, Y.M., Bedford, K.W., 1986a. Improved averaging method for turbulent flow simulation. Part 1: Theoretical development and application to Burger's transport equation. Int. J. Numer. Methods Fluids 6, 49–64.
Dakhoul, Y.M., Bedford, K.W., 1986b. Improved averaging method for turbulent flow simulation. Part 2: Calculations and verification. Int. J. Numer. Methods Fluids 6, 65–82.
Delhaye, J., 1974. Jump conditions and entropy sources in two-phase systems. Local instant formulation. Int. J. Multiphase Flow 1, 395–409.
Drew, D.A., 1983. Mathematical modeling of two-phase flow. Annu. Rev. Fluid Mech. 15, 261–291.
Drew, D.A., Lahey, R., 1987. The virtual mass and lift force on a sphere in rotating and straining inviscid flow. Int. J. Multiphase Flow 13, 113–121.
Duquennoy, C., Lebaigue, O., Magnaudet, J., 1999. Physical and numerical modelling of a gas–liquid–solid contact line. In: 37th European Two-Phase Flow Group Meeting.
Eaton, J.K., Fessler, J.R., 1994. Preferential concentration of particles by turbulence. Int. J. Multiphase Flow 16, 169–209.
Elghobashi, S., Abou-Arab, T., Rizk, M., Mostafa, A., 1984. Prediction of the particle-laden jet with a two-equation turbulence model. Int. J. Multiphase Flow 10, 687–710.
Esmaeeli, A., Tryggvason, G., 1996. An inverse energy cascade in two-dimensional low Reynolds number bubbly flows. J. Fluid Mech. 314, 315–330.
Esmaeeli, A., Tryggvason, G., 1998. Direct numerical simulations of bubbly flows. Part 1. Low Reynolds number. J. Fluid Mech. 377, 313–345.
Esmaeeli, A., Tryggvason, G., 1999. Direct numerical simulations of bubbly flows. Part 2. Moderate Reynolds number. J. Fluid Mech. 385, 325–358.
Favre, A., Kovasznay, L.S.G., Dumas, R., Gaviglio, J., Coantic, M., 1976. La turbulence en mécanique des fluides. Gauthier-Villars.
Fulgosi, M., Lakehal, D., Banerjee, S., Angelis, V.D., 2003. Direct numerical simulation of turbulence in a sheared air–water flow with a deformable interface. J. Fluid Mech. 482, 319–345.
Gueyffier, D., Li, J., Nadim, A., Scardovelli, S., Zaleski, S., 1999. Volume of fluid interface tracking with smoothed surface stress methods for three-dimensional flows. J. Comput. Phys. 152, 423–456.
Harper, J.F., 1972. The motion of bubbles and drops through liquids. Adv. Appl. Mech. 12, 59–129.
Herrmann, M., 2005. A Eulerian level set/vortex sheet method for two-phase interface dynamics. J. Comput. Phys. 203, 539–571.
Hirt, C., Nichols, B., 1981. Volume of fluid (vof) method for the dynamics of free boundaries. J. Comput. Phys. 39, 201–225.
Homescu, D., Panday, P., 1999. Forced convection condensation on a horizontal tube: influence of turbulence in the vapor and liquid phases. J. Heat Transfer 174, 874–885.
Horiuti, K., 1997. Assessment of the subgrid-scale models at low and high Reynolds numbers. In: Annual Research Briefs 1997 – Center for Turbulence Research.
Ishii, M., 1975. Thermo-fluid Dynamics Theory of Two-phase Flow. Eyrolles.
Juric, D., Tryggvason, G., 1998. Computations of boiling flows. Int. J. Multiphase Flow 24, 387–410.
Kataoka, I., 1986. Local instant formulation of two-phase flow. Int. J. Multiphase Flow 12, 745–758.
Labourasse, E., Toutant, A., Lebaigue, O., 2004. Interface–turbulence interaction. In: Proc. Int. Conf. Multiphase Flows, 2004, p. 268.
Lacanette, D., Vincent, S., Arquis, E., Gardin, P., 2002. Numerical simulation of gas-jet wiping in steel strip galvanizing process. ISIJ Int. 45, 214–220.
Lain, S., Bröder, D., Sommerfeld, M., Göz, M.F., 2002. Modelling hydrodynamics and turbulence in a bubble column using the Euler–Lagrange procedure. Int. J. Multiphase Flow 28, 1381–1407.
Lakehal, D., Smith, B.L., Milelli, M., 2002. Large-eddy simulation of bubbly turbulent shear flows. J. Turbul. 3, 025.
Lamb, H., 1993. Hydrodynamics. Dover Pubns Publishers.
Lance, M., Bataille, J., 1991. Turbulence in the liquid phase of a uniform bubbly air–water flow. J. Fluid Mech. 222, 95–118.
Lebaigue, O., Jamet, D., Duquennoy, C., Coutris, N., 1998. Review of existing methods for direct numerical simulation of liquid–vapor two-phase flows. In: 6th International Conference on Nuclear Engineering, May.
Lemonnier, H., Jamet, D., 2004. Test-case No 5: Oscillation of an inclusion immersed in a quiescent fluid. Multiphase Sci. Technol. 16, 31–38.
Lesieur, M., 1990. Turbulence in Fluids. Kluwer.
Lubin, P., Vincent, S., Caltagirone, J.P., Abadie, S., 2003. Fully three-dimensional direct numerical simulation of plunging breaking waves. C.R. Mécanique 331, 495–501.
Magnaudet, J., 1997. Simulation d'écoulements en présence d'interfaces. In: Lecture Notes, Ecole de Printemps de Mécanique des Fluides Numérique.
Magnaudet, J., 2000. The motion of high-Reynolds-number bubbles in inhomogeneous flows. Annu. Rev. Fluid Mech. 32, 659–708.
Mathieu, B., 2003. Etude physique, expérimentale et numérique des mécanismes de base intervenant dans les écoulements diphasiques. Ph.D. thesis, University of Provence.
Mathieu, B., Lebaigue, O., Tadrist, L., 2003. Dynamic contact line model applied to single bubble growth. In: 41st European Two-Phase Flow Group Meeting, May.
Menon, S., Yeung, P.K., Kim, W.W., 1996. Effect of subgrid models on the computed interscale energy transfer in isotropic turbulence. Comput. Fluids 25, 165–180.
Nicoud, F., Ducros, F., 1999. Subgrid-scale stress modelling based on the square of the velocity gradient tensor. Flow Turbul. Combust. 62, 183–200.

Peregrine, D.H., 1983. Breaking waves on beaches. Annu. Rev. Fluid Mech. 15, 149–178.
Piquet, J., 1999. Turbulence Flows Models and Physics. Springer-Verlag.
Prince, M.J., Blanch, H.W., 1990. Bubble coalescence and break-up in air-sparged bubble columns. AIChE J. 36, 1485–1499.
Sagaut, P., 2003. Large Eddy Simulation for Incompressible Flows. Springer-Verlag.
Sagaut, P., Germano, M., 2005. On the filtering paradigm for LES of flows with discontinuities. J. Turbulence 6 (23), 1–9.
Sagaut, P., Montreuil, E., Labbé, O., 1999. Assessment of some self-adaptive SGS models for wall bounded flows. Aerospace Sci. Technol. 3, 335–344.
Sato, Y., Sekoguchi, K., 1975. Liquid velocity distribution in two-phase bubble flow. Int. J. Multiphase Flow 2, 79–95.
Scardovelli, R., 1999. Direct numerical simulation of free-surface and interfacial flow. Annu. Rev. Fluid Mech. 31, 567–603.
Shen, L., Yue, D.K.P., 2001. Large-eddy simulation of free surface turbulence. J. Fluid Mech. 440, 75–116.
Smagorinsky, J., 1963. General circulation experiments with the primitive equations, I. The basic experiment. Mon. Weather Rev. 3, 99–164.
Squires, K.D., Yamazaki, H., 1995. Preferential concentration of marine particles in isotropic turbulence. Deep Sea Res. Part I: Oceanogr. Res. Papers 42, 1989–2004.
Vasilyev, O., Lund, T., Moin, P., Aksellvoll, K., 1998. A general class of commutative filters for LES in complex geometries. J. Comput. Phys. 146, 82–104.
Vincent, S., Caltagirone, J.P., 2000. A one-cell local multigrid method for solving unsteady incompressible multiphase flows. J. Comput. Phys. 163, 172–215.
Vincent, S., Caltagirone, J.P., Jamet, D., 2004a. Test-case No 15: Phase inversion in a closed box. Multiphase Sci. Technol. 16, 101–104.
Vincent, S., Caltagirone, J.P., Lubin, P., Randrianarivelo, T.N., 2004b. An adaptative augmented Lagrangian method for three-dimensional multi-material flows. Comput. Fluids 33, 1273–1289.
Vreman, B., 1995. Direct and large eddy simulation of the compressible turbulent mixing layer. Ph.D. thesis, Twente University.
Vreman, B., Geurts, B.J., Kuerten, J.G.M., 1995. A priori tests of large eddy simulation of the compressible plane mixing layer. J. Eng. Math. 29, 299–327.
Watanabe, Y., Saeki, H., 2002. Velocity field after wave breaking. Int. J. Numer. Methods Fluids 39, 281–301.
Welch, S., 1995. Local simulation of two-phase flows including interface tracking with mass transfer. J. Comput. Phys. 121, 142–154.
Yao, W., Morel, C., 2004. Volumetric interfacial area prediction in upward boiling two-phase flow. Int. J. Heat Mass Transfer 47, 307–328.
Youngs, D., 1982. Time-dependent multimaterial flow with large fluid distortion. In: Morton, K.W., Baibes, M.J. (Eds.), Numerical Methods for Fluid Dynamics, pp. 273–285.